





SUstainable solutions for affordable REtroFIT of domestic buildings

Call: H2020-LC-SC3-2018-2019-2020

Topic: LC-SC3-EE-1-2018-2019-2020

Type of action: IA

| Grant Agreement number | 894511 |
|-------------------------------|---|
| Project acronym | SUREFIT |
| Project full title | SU stainable solutions for affordable RE tro FIT of domestic buildings |
| Due date of deliverable | 31/08/2022 |
| Lead beneficiary | University of Nottingham (UNOTT) |
| Other authors | |

WP4 - Deliverable D 4.9
Results of lab testing of technologies





Dissemination Level

| PU | Public | х |
|----|--|---|
| со | Confidential, only for members of the consortium (including the Commission Services) | |
| Cl | Classified, as referred to in Commission Decision 2001/844/EC | |

Document History

| Version | Date | Authors | Description |
|---------|------------|---------------------------------|-------------------------|
| 1 | 31/08/2022 | UNOTT | First draft of D4.9 |
| 2 | 07/09/2022 | Sérgio Tadeu, Muriel Iten (ISQ) | Coordinator Review |
| 3 | 08/09/2022 | UNOTT | Final version of D4.9 |
| 4 | 04/04/2024 | UNOTT | Amended version of D4.9 |
| 5 | 09/04/2024 | Sérgio Tadeu (ISQ) | Coordinator Review |
| | | | |
| | | | |

Disclaimer

This document is the property of the **SUREFIT** Consortium.

This document may not be copied, reproduced, or modified in the whole or in the part for any purpose without written permission from the **SUREFIT** Coordinator with acceptance of the Project Consortium.

This publication was completed with the support of the European Commission under the *Horizon 2020 research and innovation programme*. The contents of this publication do not necessarily reflect the Commission's own position. The documents reflect only the author's views and the Community is not liable for any use that may be made of the information contained therein.

This project has received funding from the European Union's Horizon 2020 research and innovation programme under grant agreement No **894511**.





Contents

| T | able of figures | 4 |
|----|--|------------|
| T | able of tables | 6 |
| A | bbreviations | 7 |
| P | ublishable summary | 8 |
| In | troduction | 9 |
| 1 | Summary1 | .0 |
| 2 | Technology introduction1 | 1 |
| | 2.1 Description of the innovative technologies | L 1 |
| | 2.2 Testing conditions | L 2 |
| 3 | Methodology for lab testing1 | 4 |
| | 3.1 Bio-aerogel insulation panel | L 4 |
| | 3.2 PV vacuum glazing unit | L4 |
| | 3.3 PCM panel | ١6 |
| | 3.4 Solar assisted heat pump1 | 18 |
| | 3.5 Ground source heat pump2 | <u>!</u> 1 |
| | 3.6 Evaporative cooling unit | <u>!</u> 4 |
| | 3.7 Window heat recovery | 27 |
| | 3.8 Solar PV/T unit | 28 |
| | 3.9 Prefabricated Panels | 28 |
| 4 | Results and discussion3 | 35 |
| | 4.1 Bio-aerogel insulation panel | 35 |
| | 4.2 PV vacuum glazing unit | 36 |
| | 4.3 PCM panel | 39 |
| | 4.4 Solar assisted heat pump4 | ŀ2 |
| | 4.5 Ground source heat pump4 | 15 |
| | 4.6 Evaporative cooling unit | ١7 |
| | 4.7 Window heat recovery | ;3 |
| | 4.8 Solar PV/T unit5 | 6 |
| | 4.9 Prefabricated Panels | ;7 |
| 5. | Conclusions6 | 0 |
| R | eferences6 | i 1 |
| | | |





Table of figures

| FIGURE 1 - SUREFIT PROJECT | 9 |
|---|----|
| FIGURE 2 - U-VALUE TEST WITH INTERIOR WALL INSULATION WITH STARCH-BASED AEROGEL INSULATION PANELS | 14 |
| FIGURE 3 - THE PV VG-4L PROTOTYPE | 15 |
| FIGURE 4 - THE CALIBRATED HOT BOX WITH THE INSTALLED SAMPLE | 15 |
| FIGURE 5 - ALUMINIUM HONEYCOMB PANEL WITH INERTEK 23 AND MYLAR BAG | 16 |
| FIGURE 6 - ALUMINIUM HONEYCOMB PANEL \$23 AND ALUMINIUM COVER | 16 |
| FIGURE 7 - PLASTIC POUCH WITH S27 | 17 |
| FIGURE 8 - ALUMINIUM PANEL WITH INERTEK 23 | 17 |
| FIGURE 9 - INERTEK 23 BLISTER PANEL | 17 |
| FIGURE 10 - A28 BLISTER PANEL IN TEST | 18 |
| FIGURE 11 - TEST RIG OF THE SAHP | 19 |
| FIGURE 12 - HOT WATER STORAGE TANK | 19 |
| FIGURE 13 - SOLAR RADIATION SIMULATOR AND LIGHT REGULATOR | 20 |
| FIGURE 14 - WORKING SAMPLE OF THE THERMODYNAMIC PANELS | 21 |
| FIGURE 15 - ELECTRO-OSMOSIS DAMP PROOF MONITOR | 22 |
| FIGURE 16 - GRAPHITE PARTICULAR | |
| FIGURE 17 - DT85 DATA LOGGER, K-THERMOCOUPLES, FLOW METER, HAND HELP THERMOMETER, AND AIR FLOWMETER | 23 |
| FIGURE 18 - THE TEST RIG OF THE NOVEL CROSS FLOW HOLLOW FIBRE INTEGRATED EVAPORATIVE COOLING MODULE (A) AND THE | |
| CONNECTIONS WITH THE ENVIRONMENTAL CHAMBER (B) | |
| FIGURE 19 - THE 3-D MODEL IMAGE OF THE HOLLOW FIBRE MODULE CORE DESIGN | 25 |
| FIGURE 20 - CORE STRUCTURE OF SINGLE UNIT FOR BOTH EVAPORATIVE COOLING AND DESICCANT DEHUMIDIFICATION | |
| FIGURE 21 - WINDOW HEAT RECOVERY PROTOTYPE USED IN THE EXPERIMENTS | |
| FIGURE 22 - INSTALLATION STEPS OF PWI PANEL | |
| FIGURE 23 - POST-RETROFIT RENDERING EFFECTS | |
| FIGURE 24 - STRUCTURE OF PANEL 1(LEFT: AXONOMETRIC VIEW; RIGHT: CROSS-SECTIONAL VIEW) | |
| FIGURE 25 - STRUCTURE OF PANEL 2 (LEFT: AXONOMETRIC VIEW; RIGHT: CROSS-SECTIONAL VIEW) | |
| FIGURE 26 - STRUCTURE OF PANEL 3 (LEFT: AXONOMETRIC VIEW; RIGHT: CROSS-SECTIONAL VIEW) | |
| FIGURE 27 - STRUCTURE OF PANEL 4 (LEFT: AXONOMETRIC VIEW; RIGHT: CROSS-SECTIONAL VIEW) | |
| FIGURE 28 - STRUCTURE OF PANEL 5 (LEFT: AXONOMETRIC VIEW; RIGHT: CROSS-SECTIONAL VIEW) | |
| FIGURE 29 - THE CONCEPT AND STRUCTURE OF HOT BOX | |
| FIGURE 30 - THE TESTING RIG CONDITION | |
| FIGURE 31 - U-VALUE OF INTERIOR WALL WITH STARCH-BASED AEROGEL INSULATION PANELS (72 CONTINUOUS NIGHTS) | |
| FIGURE 32 - THERMAL COMFORT WITH STARCH-BASED AEROGEL BASED VACUUM INSULATION PANELS (72 CONTINUOUS NIGHTS) | |
| FIGURE 33 - SOLAR AND ELECTRICITY CONVERSION EFFICIENCY WITH TESTING OF PV VG-4L | |
| FIGURE 34 - PV ELECTRICITY CONVERSION EFFICIENCY WITH SOLAR RADIATION | |
| FIGURE 35 - U-VALUE OF PV VG-4L IN DIFFERENT TIME PERIODS (A) (B) (C) | |
| FIGURE 36 - TEST RESULTS | |
| FIGURE 37 - BLISTER PCM PANEL PROTOTYPE | |
| FIGURE 38 - THIN ICE PANEL | |
| FIGURE 39 - TEST ROOM | |
| FIGURE 40 - ROOM TEMPERATURE WITHOUT PCM AND RADIATOR FOR HEATING | |
| FIGURE 41 - ROOM TEMPERATURE COMPARISON | |
| FIGURE 42 - ROOM PRE HEATED AND THEN HEATING TURNED OFF FOR DURATION OF TEST | |
| FIGURE 43 - SUMMARY OF SYSTEM COP. | |
| FIGURE 44 - LINEAR REGRESSION OF COPH AS FUNCTION OF T _P FOR THE FOUR DIFFERENT PILOTS. | |
| FIGURE 45 - ENERGY FLOW WORK SIMULATION PROCESS IN ENERGYPRO SOFTWARE | |
| FIGURE 46 - HEATING COP OF SOLE SAHP AND PV-SAHP-TS INTEGRATED SYSTEMS | 45 |





| -IGURE 47 - AVERAGED RESULTS FOR EACH MOISTURE FACTOR | 40 |
|---|-------------------|
| FIGURE 48 - EFFECT OF INLET AIR TEMPERATURE ON OUTLET AIR HUMIDITY AND SOLUTION TEMPERATURE | 49 |
| FIGURE 49 - EFFECT OF INLET AIR RELATIVE HUMIDITY ON OUTLET AIR HUMIDITY AND SOLUTION CONCENTRATION | 50 |
| FIGURE 50 - EFFECT OF AIR MASS FLOW RATE ON OUTLET AIR TEMPERATURE/HUMIDITY AND SOLUTION CONCENTRATION | 50 |
| FIGURE 51 - Effect of solution mass flow rate on outlet air temperature/humidity and solution concentration | 51 |
| Figure 52 - Effect of solution inlet temperature on outlet air temperature/humidity and solution concentration | 51 |
| FIGURE 53 - EFFECT OF SOLUTION CONCENTRATION AND INLET AIR TEMPERATURE ON OUTLET RELATIVE HUMIDITY | 52 |
| FIGURE 54 - HYBRID SYSTEM COP WITH VARIABLES OF INLET AIR TEMPERATURE AND RELATIVE HUMIDITY | 53 |
| FIGURE 55 - COMPARISON BETWEEN EXPERIMENTAL AND NUMERICAL RESULTS FOR DIFFERENT TEST CONDITIONS | 54 |
| FIGURE 56 - IMPACT OF MAXIMUM TEMPERATURE DIFFERENCE ON THE THERMAL EFFECTIVENESS WITH VENTILATION RATE VARIED | |
| ветween 10 то 60 м³/н | 55 |
| FIGURE 57 - I MPACT OF HEAT PIPE NUMBERS ON THE THERMAL EFFECTIVENESS WITH VENTILATION RATE VARIED BETWEEN 10 to 60 M | 1 ³ /H |
| | 56 |
| Figure 58 - a) Hourly variation of PV, ambient, water temperatures and incident solar radiation, b) effect of poly HE | ON |
| POWER CONVERSION EFFICIENCY AND C) USEFUL HEAT GAIN | 57 |
| FIGURE 59 - TESTING TEMPERATURE DISTRIBUTION OF (A) PANEL 1; (B) PANEL 2; (C) PANEL 3; (D) PANEL 4 AND (E) PANEL 5 | 59 |





Table of tables

| TABLE 1 - INTRODUCTION OF THE SIMULATION RESULTS OF EACH TECHNOLOGY | 11 |
|---|------------|
| TABLE 2 - TESTING CONDITIONS AND STANDARDS FOR EACH TECHNOLOGY | 12 |
| TABLE 3 - MEASUREMENT DEVICES AND THEIR ACCURACY | 18 |
| TABLE 4 - GEOLOGY AND RESULTS FOR THERMAL RESPONSE TESTS CARRIED OUT | 23 |
| TABLE 5 - SPECIFICATIONS OF PANEL 1 | |
| TABLE 6 - SPECIFICATIONS OF PANEL 2 | 31 |
| TABLE 7 - SPECIFICATIONS OF PANEL 3 | 31 |
| Table 8 - Specifications of panel 4 | 32 |
| Table 9 - Specifications of Panel 5 | <i>3</i> 3 |
| Table 10 -Building heating demand and imported electricity with sole SAHP system | 44 |
| Table 11 - Building heating demand and imported/exported electricity with PV-SAHP-TS system | 45 |
| TABLE 12 - ENERGY PERFORMANCE RESULTS OF 3KW AND 6KW HEATING CAPACITY | 46 |
| Table 13 - Comparison between measurements and numerical for $ma=57~\text{m}^3/\text{H}.$ | 47 |
| Table 14 - Comparison between measurements and numerical for $ma=114~\text{m}^3/\text{h}$ | 48 |
| Table 15 - Comparison between measurements and numerical for $ma=171~\text{m}^3/\text{h}$ | 48 |
| TABLE 16 THERMAL COP FOR DIFFERENT INLET TEMPERATURE AND RELATIVE HUMIDITY | 52 |
| TABLE 17 ELECTRICAL COP FOR DIFFERENT INLET TEMPERATURE AND RELATIVE HUMIDITY | 52 |
| TABLE 18 -COMPARISON BETWEEN MEASURED AND MODELLED OUTLET TEMPERATURE | 54 |
| TABLE 19 - VALIDATION OF U AND R VALUES | 58 |



Abbreviations

SAHP Solar-assisted heat pump

GSHP ground source heat pump

WHR window heat recovery

PV/T Photovoltaics and thermal

COP Coefficient of Performance

EER Energy efficient rate

HP Heat pipe

 $arepsilon_{sen}$ Sensible effectiveness

 $arepsilon_{lat}$ Latent effectiveness



Publishable summary

This report is focused on the testing the performance of the technologies under laboratory controlled conditions to simulate different climatic and operating conditions by all the partners involved with bulk of the testing by UNOTT, AALTO and ISQ. The achieved results will be used to modify the design of technologies. Results will be used to prefabricate the renovation technologies appropriate for each building and climate in Task 4.4.





Introduction

Leading Beneficiary: UNOTT

Participants: AALTO, ISQ, CJR

Task description:

Task 4.3: Test the performance of the technologies under laboratory-controlled conditions (UNOTT, M15-M23). The innovative technologies will be tested under controlled conditions; the achieved results will be used to modify the design of technologies, if necessary. The tests will be conducted in the laboratories to simulate different climatic and operating conditions by all the partners involved with bulk of the testing by UNOTT, AALTO, CJR and ISQ.



Figure 1 - SUREFIT PROJECT





1 Summary

The work package involves fabricating and testing the key components and assembling the components into complete prototypes of technologies. The technologies will be tested in the lab to assess their performance under the nominal set conditions. The testing results will be used to modify and improve the design of the final prototypes, if necessary, which will be used in WP6 (field tests). The availability of this prototype system for field trials will be milestone 3.

The innovative technologies will be tested under controlled conditions; the achieved results will be used to modify the design of technologies, if necessary. The tests will be conducted in the laboratories to simulate different climatic and operating conditions by all the partners involved with bulk of the testing by UNOTT, AALTO, CJR and ISQ.





2 Technology introduction

There were eight innovative retrofit technologies selected for the five building pilots: Finland, Greece, Portugal, Spain and the United Kingdom. All the buildings were old residential buildings that did not meet current energy efficiency standards. The Bio-aerogel insulation panel, PV Vacuum glazing unit, PCM panel are used to reduce the heating demand by improving the façade performance. The solar-assisted heat pump, ground source heat pump, evaporative cooling unit and window heat recovery unit are used for energy efficient space heating/cooling and ventilation and domestic hot water generation systems. During the M7 to M23, mathematical models have been generated to simulate the energy performance of those technologies, as described in D4.1 to D4.8. In this deliverable, the simulation results will be validated and optimized via the experimental tests.

2.1 Description of the innovative technologies

The simulation results and relative partners of each technology are introduced in Table 1.

Table 1 - Introduction of the simulation results of each technology

| Technology | Partner (developer) | Simulation results |
|------------------------------|------------------------|--|
| Bio-aerogel insulation panel | UNOTT, WINCO, CJR | Thermal conductivity: 0.024 W/m·K |
| PV Vacuum glazing unit | UNOTT | U-value=0.56 W/m ² ·K, solar to electricity conversion factor: 4% at 50% transparency |
| PCM panel | PCM, CJR | 220kJ/kg latent heat capacity with melting temperature between 23-27°C |
| Solar-assisted heat pump | UNOTT | System heating COP ranging from 2.8 to 3.8 with varied solar radiation |
| Ground source heat pump | UNOTT | The ground heat exchanger thermal conductivity improved by 93%, with heating COP varied from 3.81 to 4.48 depending on different soil temperature |
| Evaporative cooling unit | UNOTT | The air outlet temperature of 22.4°C, 61.7% achieved when inlet air temperature is 30°C with relative humidity of 80%. The cooling energy efficiency is predicted at 3.65, with cooling capacity varied from 434W to 1534W and moisture remove rate varied from 1.02kg/s to 2.76kg/s |





| Window heat recovery | UNOTT | Thermal recovery efficiency higher than 73% depending on the temperature differences of the heat pipe condensing and evaporating sides |
|----------------------|------------|--|
| Solar PV/T unit | SOLIMPKES | Solar to electricity conversion efficiency: 20% (315 W per unit). Solar to thermal conversion efficiency: 47% (855 W per unit) |
| Prefabricated Panels | CJR, UNOTT | U-value achieved: 0.19-0.35 W/m ² ·K with different core integration |

2.2 Testing conditions

The testing conditions and standards for each technology are illustrated in *Table 2*.

Table 2 - Testing conditions and standards for each technology

| Technology | Testing conditions | |
|------------------------------|--|--|
| Bio-aerogel insulation panel | Testing the U-value of the insulation material under the winte conditions with air temperature differences higher than 20°C | |
| PV Vacuum glazing unit | Testing the solar electricity under different solar radiation varied from 0 to 600W/m ² | |
| PCM panel | Testing the charging and discharging time, as well as temperature drop under the melting periods | |
| Solar-assisted heat pump | Testing under different solar radiation varied from 0 to 700W/m², with wind speed varied from 0 to 2m/s and ambient air temperature from 5°C to 30°C | |
| Ground source heat pump | Testing the soil side heat exchanger efficiency and the overall COP under different soil temperature | |
| Evaporative cooling unit | Testing the cooling performance under different inlet ai temperature from 25°C to 33°C and relative humidity from 55% to 75%, as well as the inlet air flow rate of 57-171m³/s | |
| Window heat recovery | Testing the heat recovery efficiency under temperature differences of 5°C, 10°C, 15°C and 20°C | |
| Solar PV/T unit | Testing the effective PV module temperature and was temperature with the ambient temperature and the incid solar radiation | |





| Prefabricated Panels | Testing the U-value of the prefabricated insulation panels with air temperature differences of 30°C with the guideline in ISO |
|----------------------|---|
| | 12567 |





3 Methodology for lab testing

3.1 Bio-aerogel insulation panel

The starch-based aerogel insulation panels with thickness of 45mm and surface of 0.123m² (0.35m×0.35m) is installed on part of the experiment wall, which is compared with original wall part without insulation panels. One heat flux sensor is installed on the surface of the interior insulation panel, with another one installed on the original wall part, which has 200mm distance away from the edge of the insulation panels.

To investigate the performance with installation of starch-based aerogel insulation Panel on the interior wall, 3 successive days (72hours) are carried out from 2nd December 2021 to 5th December 2021. The installed samples are shown in *Figure 2*, as well as the thermograph imaging, which indicates the air temperature with 30mm distance from the panel central point is approximately 35.3°C.



Figure 2 - U-value test with interior wall insulation with starch-based aerogel insulation panels

3.2 PV vacuum glazing unit

A PV VG-4L prototype using an amorphous silicon (α -Si) solar cell, as shown in *Figure 3*, was manufactured. The U-value of the prototype was evaluated using the TEC-driven calibrated hot box built at the University of Nottingham. As can be seen in Figure 3, by following closely ISO 12567 standards, the sample was installed at the specimen area of the calibrated hot box. It was tested under three different air temperature conditions from 7.6°C to 12.7°C of external air temperature and 27.8°C to 32.7°C of internal air temperature. However, the air speed in the hot and cold side were fixed at 0.3 m/s and 1.5 m/s respectively. Using the calibrated hot box, we could estimate the total heat transfer coefficient from the hot and cold surface of the PV VG-4L prototype. The values were then used as the input parameters for the computer simulation. To derive the absolute error, the Kline–McClintock second power law as given in NCEES (National Council of Examiners for Engineering and Surveying) (2001) is used. These errors were represented by the error bars of the associated curves. Additionally, the guideline in ISO 12567 was also being referred to evaluate the error from indoor testing.







Figure 3 - The PV VG-4L prototype

The mathematical model validation method is performed by comparing the results obtained experimentally and theoretically, based on the trends shown on the related graphs. In this study, the mathematical model has been validated, with the input parameters recorded in the experiment of all the three different conditions. In addition to the direct comparison between the simulation and theoretical curves, the validation of the mathematical model is further justified using root mean square percentage deviation (RMSPD). As shown in *Figure 4*, the evaluated glazing surface temperatures and U-value are found to be in good agreement with the temperatures and U-value accuracy of only 4.02% and 0.92% respectively.





Figure 4 - The calibrated hot box with the installed sample





3.3 PCM panel

As previously stated, PCMs with melting temperature in the range of 18°C-29°C are considered for adoption in the built environment.

Prototype panels were developed using a selection of PCM materials, with various phase change temperatures. The initial concepts were produced and tested at University of Nottingham. Different testing materials are displayed from *Figure 5* to *Figure 9*. And the installed PCM panels in the testing room is shown in *Figure 10*.

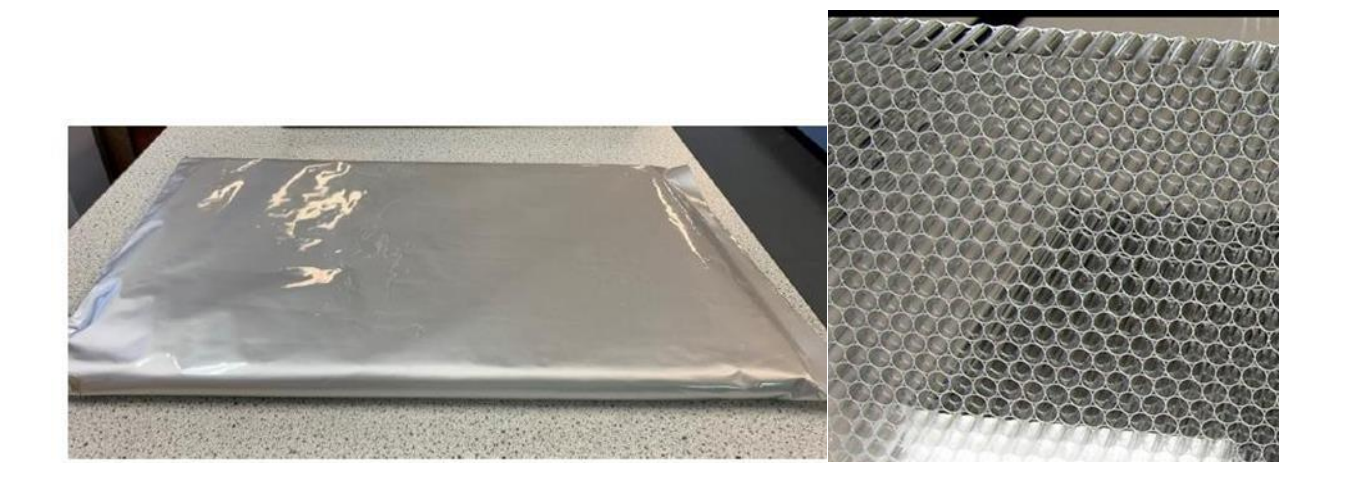


Figure 5 - Aluminium honeycomb panel with INERTEK 23 and Mylar Bag



Figure 6 - Aluminium Honeycomb panel S23 and aluminium cover





Figure 7 - Plastic pouch with S27





Figure 8 - Aluminium panel with INERTEK 23



Figure 9 - INERTEK 23 blister panel







Figure 10 - A28 Blister panel in test

3.4 Solar assisted heat pump

The experiments are carried out in University of Nottingham, with the dynamic panels installed vertical. The overall SAHP system is connecting with an existed hot water storage tank, to provide both hot water and space heating for the occupants. The test rig is shown in Figure 11. Inlet, outlet and tank-central water temperatures of hot water tanks are tested with K type thermocouples. Inlet and outlet air temperatures from the ventilation machine are tested with K type thermocouples. Besides, the air supply velocity is measured with Testo thermo-anemometer. Finally, a DT500 data logger collected all the data from the above sensors. Detailed information about the measure sensors, including the measurement accuracy and measurement range are shown in Table 3.

Table 3 - Measurement devices and their accuracy

| Instrumentation | Measured parameter | Measurement range | Accuracy |
|-------------------------------|---------------------------|------------------------|----------|
| Testo thermo- anemometer | Air velocity | 0–10 m/s | ±5% |
| K-type thermocouple | Water and air temperature | 0-1100 °C | ±0.75% |
| Datalogger DT500 | Data Acquisition | N/A | ±0.15% |
| KIPP & ZONEN Pyranometer CMP3 | Solar radiation | 0-2000W/m ² | ±5% |
| NEVSETPO Power meters | Electricity consumption | 0-2900W | ±4% |



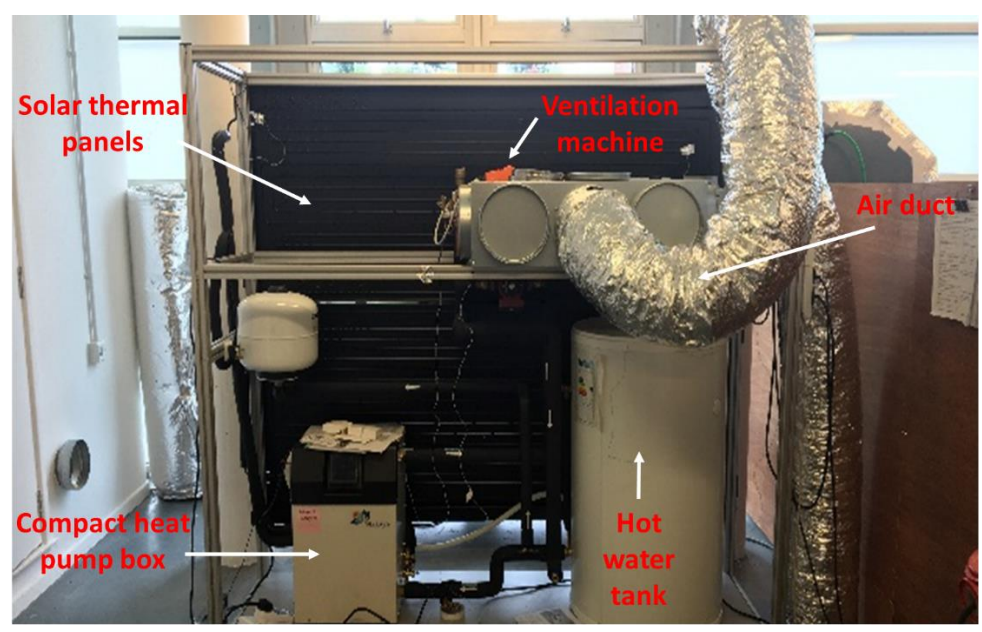


Figure 11 - Test rig of the SAHP

The jacket containing the pure water is used to store and release the heat produced from the condenser of the SAHP system. The jacket is based on the single tank (HWT) configuration, which is shown in Figure 12. The existing SAHP retains its immersion heater for energy input connected to the hot water supply which is based on a heat pump coupled to ternary evaporator panels located in the loft space and exterior roof.



Figure 12 - Hot water storage tank

To simulate solar radiation under laboratory conditions, an artificial portable light source combining metal-halide and thirty tungsten halogen floodlights source is assembled. The main reason of the solar simulator is to deliver a controllable indoor sun light for the heat pump system. This adjustable illuminate with wavelength ranges between 360-2500 nm and regulator switch, solar irradiance in the range 0 to 800 W/m² covering an area of 3.2m² as shown in *Figure* 13. The switch acts as a regulator in order to maintain solar irradiance variations evenly. The





collector is placed indoor up-right in the lab, 200 cm distance in the front of the solar simulator to achieve the required operational conditions. In this case unevenness values at most points obtained is found less than 9%, which is in a good agreement with the British Standards values for indoor solar simulator. The working sample of thermodynamic panels is shown in *Figure 14*.

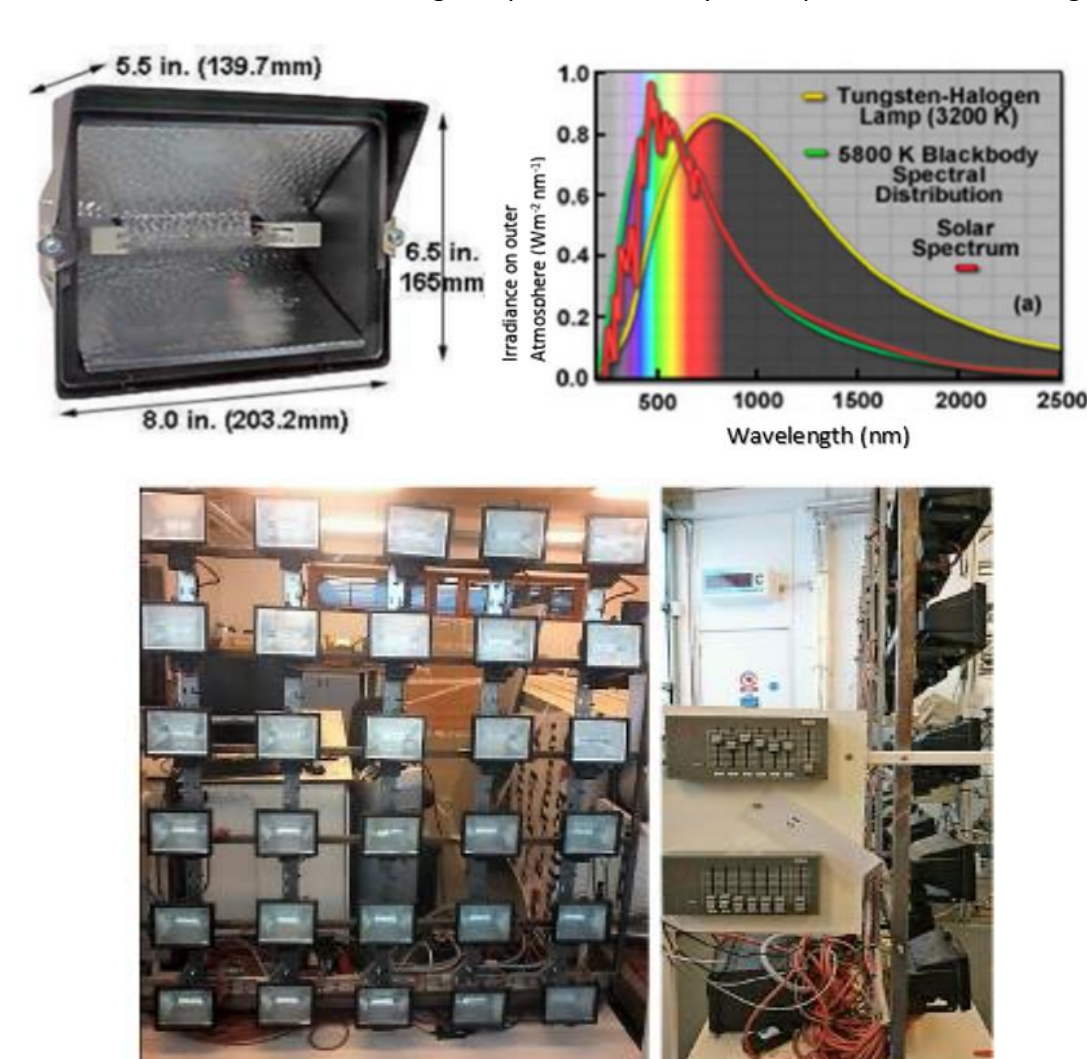


Figure 13 - Solar radiation simulator and light regulator







Figure 14 - Working sample of the thermodynamic panels

3.5 Ground source heat pump

The purpose of these experiments is to determine the impact of introducing graphite particles into different types of soils. The thermal conductivity is an intensive property, meaning that it is independent of system size.

A KD2 Pro Thermal Properties Analyzer was used to measure the thermal conductivity of samples. Samples of the three main types of soil were obtained including: Loam, Sandy & Clay. These samples were dried in an oven for over 12 hours at 115°C to ensure that all traces of water were removed. These samples were then weighed and prepared.

The wet weight of the soil was determined by the following equation:

Wet weight
$$(g) = Dry \ weight \ (g) \times \left(\frac{1}{(1 - Moisture \ Factor)}\right)$$

The added water for a given test was evenly mixed into the soil to obtain the test sample. This was then transferred into a container and compressed with a 500g weight to ensure that soil compression does not influence results. The probe was then inserted into the sample. Three measurements of thermal conductivity were taken, with the TR-1 sensor which was designed for use with soil.

For the tests with the graphite enhancement, 3wt% of graphite was introduced to the moistened soil before taking measurements.

Osmosis damp proofing uses a series of anodes placed at the base of the wall and a cathode rod buried at a lower level in the ground (*Figure 15*). This electric damp proof course imparts a small electrical charge into the masonry and this positive charge repels free moisture molecules from the anodes where they are attracted to the negative cathodic earth rod.





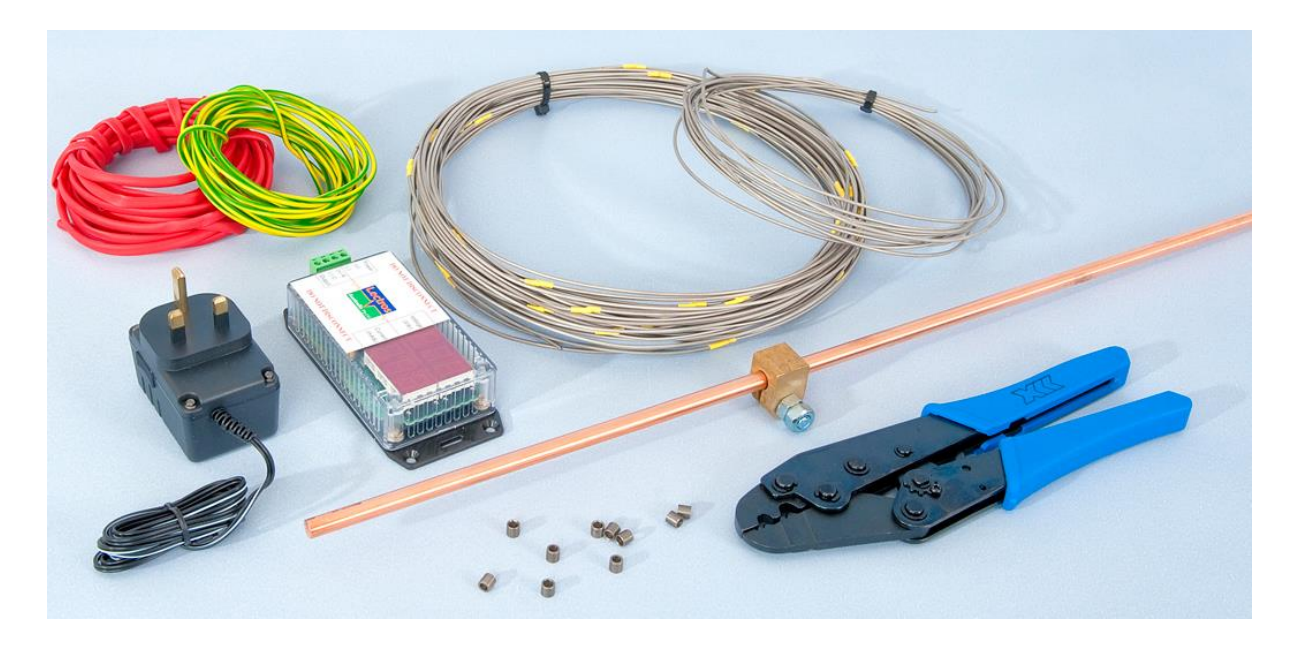


Figure 15 - Electro-Osmosis Damp Proof Monitor



Figure 16 - Graphite particular

Graphite (*Figure 16*) has the same chemical composition as Diamond, which is also pure carbon, but the molecular structure of Graphite and Diamond is entirely different. The test equipment is shown in *Figure 17*.











Figure 17 - DT85 data logger, K-thermocouples, Flow meter, Hand help thermometer, and Air flowmeter.

In most region of Europe including of the UK, the seasonal ground temperatures remain relatively constant beyond a depth of 10m. Values between 6°C and 12°C predominate to a depth of about 15m, and then 12°C-15°C predominates to a depth of about 50m. Such temperatures represent ideal conditions to permit economical space and water heating by using energy piles structures and heat pumps. Substantial temperature fluctuations in summer and winter during the year would reduce the efficiency of heat pump systems. The soil battery functions as the thermal energy storage using energy piles in the residential sectors is an existing technology but not yet proven in the UK, one of the drawbacks could be because of the extremely variable characteristics of the UK ground that is used to balance winter cold and summer heat gain by storing heat. One of the purposes of the further work from this project could be to investigate the capability of UK soil to store heat. *Table 4* represents for the geology and results for thermal response tests carried out.

Table 4 - Geology and results for thermal response tests carried out

| Geology | Thermal conductivity, λ_{eff} (W/m K) | Resistance, Rb (K/(W/m)) |
|---------------------------------------|---|--------------------------|
| Silt and clay (Quarternary/Tertiary) | 1.6 | _ |
| Mesozoic sediments | 2.7-2.8 | 0.10-0.18 |
| Marl ("Emschermergel", Cretaceous) | 1.5-2.0 | 0.11-0.12 |
| Sand/silt, marl (Cretaceous) | 2.3 | 0.08^{a} |
| Sand and clay (Quarternary/Tertiary) | 2.8 | 0.11 |
| Sand and clay (Quarternary/Tertiary) | 2.2-2.3 | $0.07-0.08^{a}$ |
| Marl, clayey | 2.5 | 0.12 |
| Marl, sandstone, limestone (Mesozoic) | 4.0 | 0.08^{a} |
| Silt, sandy (Quarternary/Tertiary) | 3.4 | 0.06^{a} |

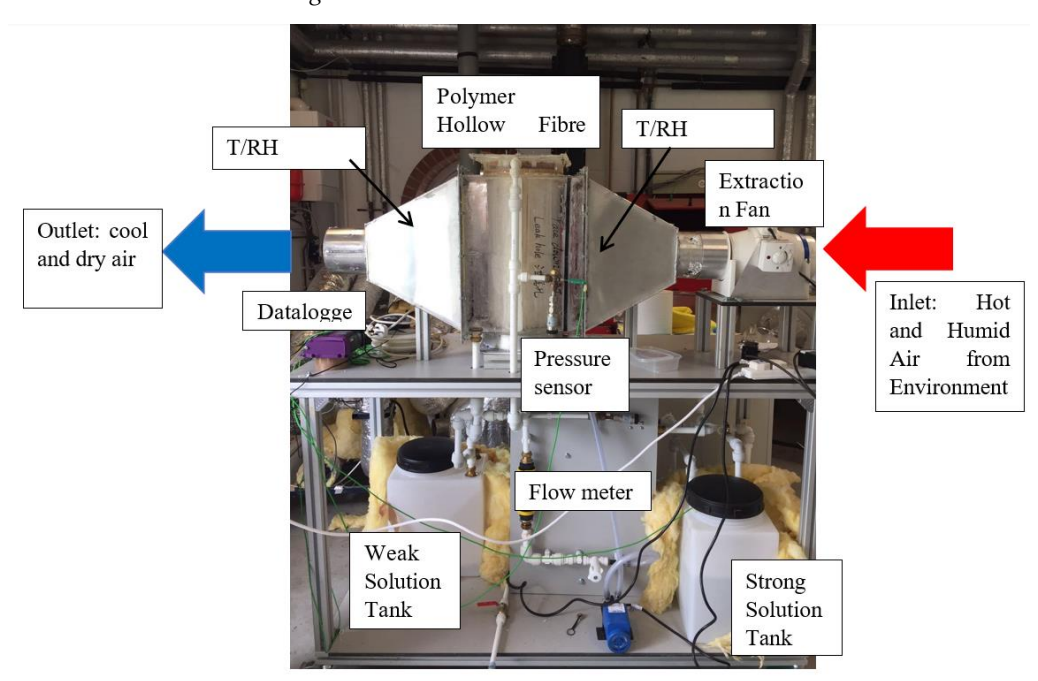
^aFilled with thermally enhanced grout ("Stüwatherm").



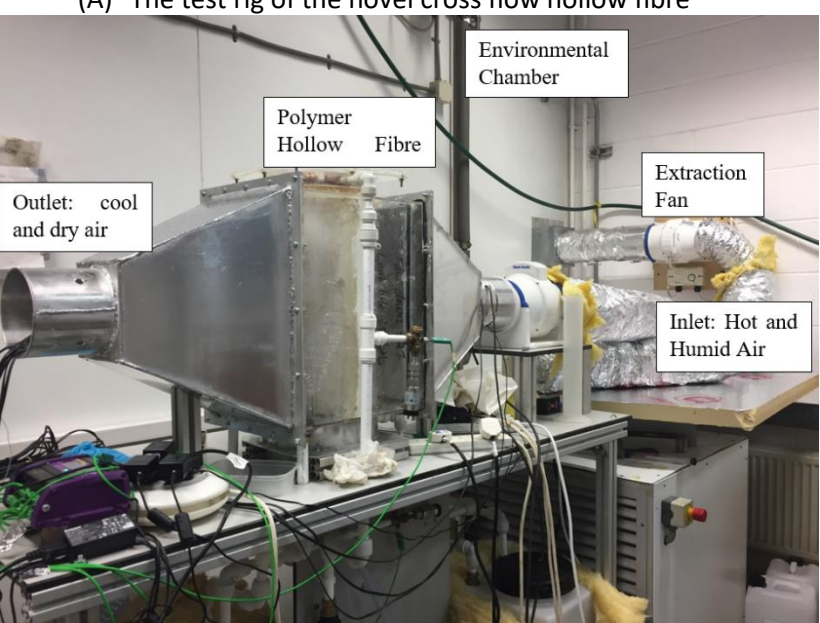


3.6 Evaporative cooling unit

The performance tests for the design concept are separated into two different units, including an air dehumidification unit with liquid desiccant solutions of potassium format (KCOOH), and a water evaporative cooling unit. The two different functional units have the same physical structure as shown in *Figure 18*, with difference of liquid fluent. The hollow fiber module core is designed with 3D structure modelled in *Figure 19*.



(A) The test rig of the novel cross flow hollow fibre



(B) Connections with the environmental chamber

Figure 18 - The test rig of the novel cross flow hollow fibre integrated evaporative cooling module (A) and the connections with the environmental chamber (B)





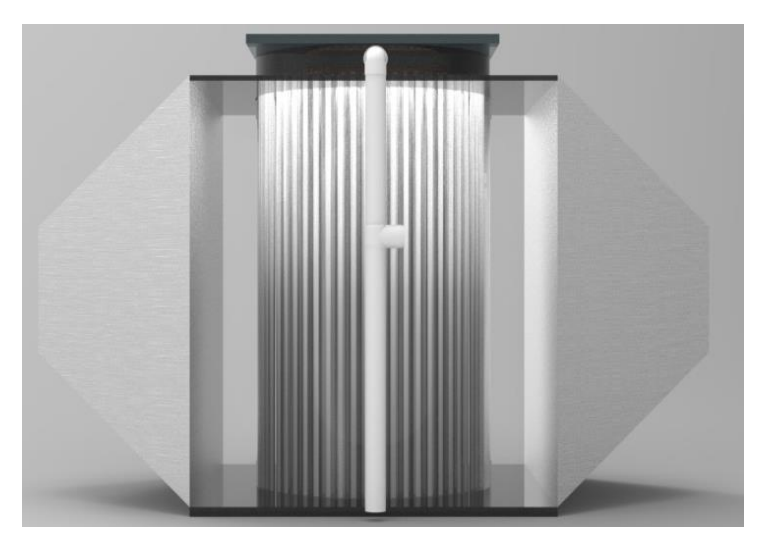


Figure 19 - The 3-D model image of the hollow fibre module core design

At the beginning of each test, the environmental chamber was set to the required temperature and humidity level. As soon as the temperature and humidity reached the desired values, the solution/water circulation pump and the fan in the air stream direction will be switched on. The air velocity is measured at five different positions along the cross sections of the outlet aluminium tunnel, using the air velocity probes connected to a recorder (Testo 454). In order to minimize the experimental testing errors, four humidity and temperature sensors (EK-H4, Sensirion, UK) were located at the inlet (point 1 in *Figure 20*) and outlet (point 2 in *Figure 20*) of the air stream respectively, to measure the inlet and outlet conditions of the air stream. Additional K type thermocouples were used to measure the temperature of the desiccant solution entering and leaving the hollow fibre module. The aluminium air tunnel was connected with a variable frequency drive centrifugal fan, which was linked directly with the environmental chamber. A centrifugal pump was employed to circulate solution/water from the solution/water tank to the top of the hollow fiber module. 8 nozzles were allocated at the top of the module with the aim to make sure the cross section of the hollow fiber module could be wetted entirely.





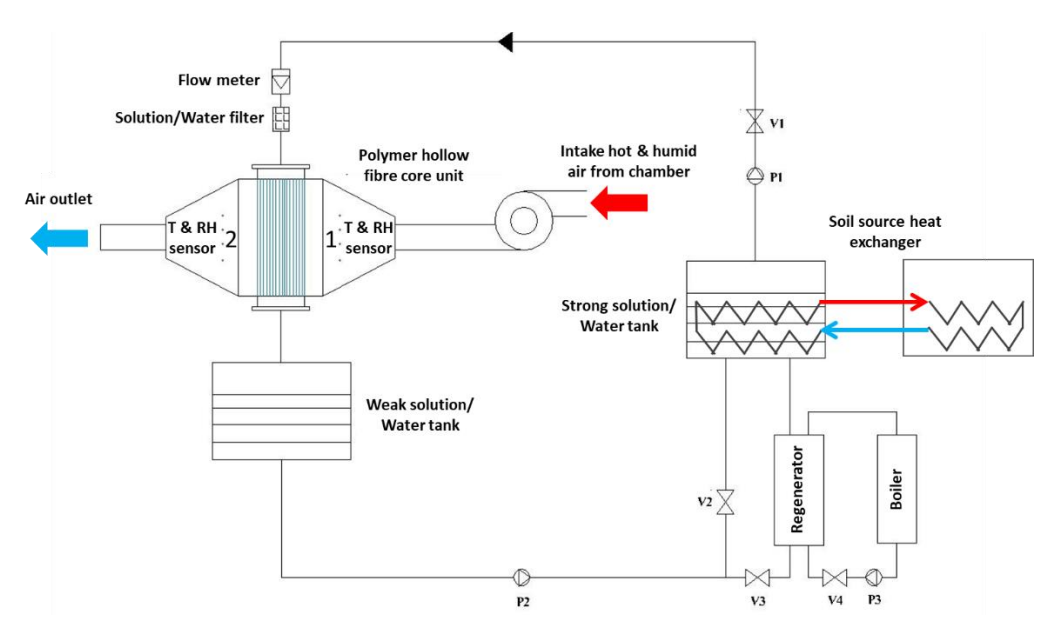


Figure 20 - Core structure of single unit for both evaporative cooling and desiccant dehumidification

For each test, the temperature and humidity values were recorded every 20 seconds until the time when the system reached steady states as indicated by the humidity and temperature sensor readings. The accuracy of the measuring instruments used was: $\pm 0.2\%$ for temperature, $\pm 0.5\%$ for pressure, $\pm 2\%$ for air velocity, and $\pm 2\%$ for relative humidity.

Air side effectiveness has been widely applied to evaluate the performance of dehumidification and cooling process. The performance of the system is found through calculation of the sensible effectiveness (ε_{sen}) and latent effectiveness (ε_{lat}) .

The air side sensible heat effectiveness (ε_{sen}) is an important parameter to evaluate the heat transfer performance between the intake air and the inside solution fluid. This is defined as the ratio between the actual temperature change of the air passing through the hollow fibres ($T_{a,in} - T_{a,out}$), and the maximum possible temperature difference in the hollow fibre units ($T_{a,in} - T_{sol,in}$):

$$\varepsilon_{sen} = \frac{T_{a,in} - T_{a,out}}{T_{a,in} - T_{sol,in}}$$

Where, $T_{a,in}$ and $T_{a,out}$ represents the inlet and outlet air dry-bulb temperature. $T_{sol,in}$ represents for the temperature of inlet solutions.

The air side latent heat effectiveness (ε_{lat}) is significant to evaluate the mass transfer performance or moisture remove effectiveness of the air. Because of the water vapour pressure difference, the hot air with high humidity will transport the water into the inside of the hollow fibres. In the process, the water vapour can pass through the micro porous on the surface of the hollow fibres, and the water changes from vapour to liquid. This is defined as the ratio between the actual ($\omega_{a,in}-\omega_{a,out}$) and maximum possible difference of the specific humidity ($\omega_{a,in}-\omega_{eq}$):





$$\varepsilon_{lat} = \frac{\omega_{a,in} - \omega_{a,out}}{\omega_{a,in} - \omega_{eq}}$$

Where, $\omega_{a,in}$ and $\omega_{a,out}$ is the relative humidity of inlet air and outlet air. ω_{eq} is the equilibrium humidity ratio of air at the inlet condition of the desiccant solution, of which the vapour pressure is a function of concentration and temperature of the solution (Chen et al., 2018), which is calculated as below

$$\omega_{eq} = 0.622 \frac{P_{sol}(X_{sol}, T_{sol})}{P_{atm} - P_{sol}(X_{sol}, T_{sol})}$$

Where, P_{atm} is the atmospheric pressure; P_{sol} is the vapour pressure of desiccant solution at the specific concentration X_{sol} and temperature T_{sol} . The desiccant solution concentration X_{sol} can be determined by the solution temperature and density. P_{sol} can be calculated with the empirical correlation derived by Cisternas and Lam (Cisternas and Lam, 1991), as shown below:

$$\log P_{sol} = K \cdot \left[A - \frac{B}{T - E_s} \right] + \left[C - \frac{D}{T - E_s} \right]$$

Where P_{sol} is the solution equilibrium vapour pressure (kPa); I is the molar concentration (mol/kg); K is an electrolyte parameter relating to solute (KCOOH); A, B, C, D and E_s are parameters regarding to solvent (water).

Regarding the performance of the regenerative cycle, it can be obtained through calculation of thermal COP_{th} and electrical COP_{elec} , defined, respectively, as:

$$COP_{th} = \frac{Q_a}{Q_{in}}$$

$$COP_{elec} = \frac{Q_a}{W_p + W_f}$$

where Q_a is the cooling capacity (sensible and latent), Q_{in} is the input of thermal energy to cycle (from the solar thermal collector) and W_p and W_f are the total electric power consumed in the pumps and fans, respectively.

3.7 Window heat recovery

The window heat recovery prototype presented in *Figure 21* was tested under different conditions. The temperature was recorded in different locations, as identified in *Figure 21* (T_1 to T_9 are temperature sensors), and then the average temperature on the two sides of the pipes and the average heat flux are calculated.





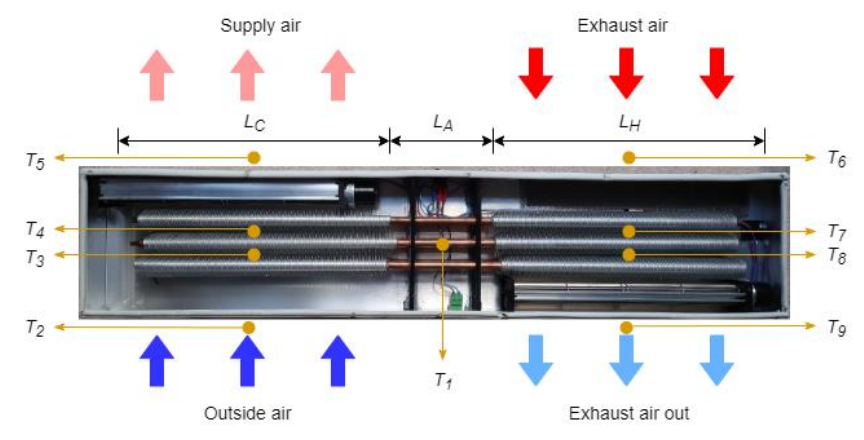


Figure 21 - Window heat recovery prototype used in the experiments

3.8 Solar PV/T unit

The test of the PV/T system is conducted in Marmont Laboratory, University of Nottingham. The wind speed was observed over the course of test to detect the heat flow rate through natural convection between the PV panels and ambient air, and was measured as 1.2 m/s in average. Also, average solar radiation data during the day and outside air temperature were found to be 761.5 W/m²and 37.2 °C, respectively. During the series of test sessions, no working fluid leakage was observed both in the roof and cooling units.

3.9 Prefabricated Panels

The installation process for prefabricated wall insulation panels typically involves several steps to ensure proper placement and effective insulation, with the installation steps illustrated in Figure 22. During the preparation step, it is pivotal to remove any existing wall finishes, such as drywall or cladding, as necessary. Also, it is important to ensure that the wall surface is clean, dry, and free from debris. Then, the metal framework should be positioned on the wall surface. Moreover, the PWI panels should then be adhered to and filled in the metal framework with the measured dimensions of the wall to accurately to determine the required size of the insulation panels. Once the panels are positioned correctly, secure the panels to the wall using appropriate fasteners. After the insulation panels are securely in place, the wall finishing could be rendered according to versatile preferences (textures, colours, etc.), as shown in *Figure 23*. Once the installation is complete, quality check should be conducted thoroughly to ensure that the insulation panels are properly installed, with no gaps, loose sections, or visible defects.





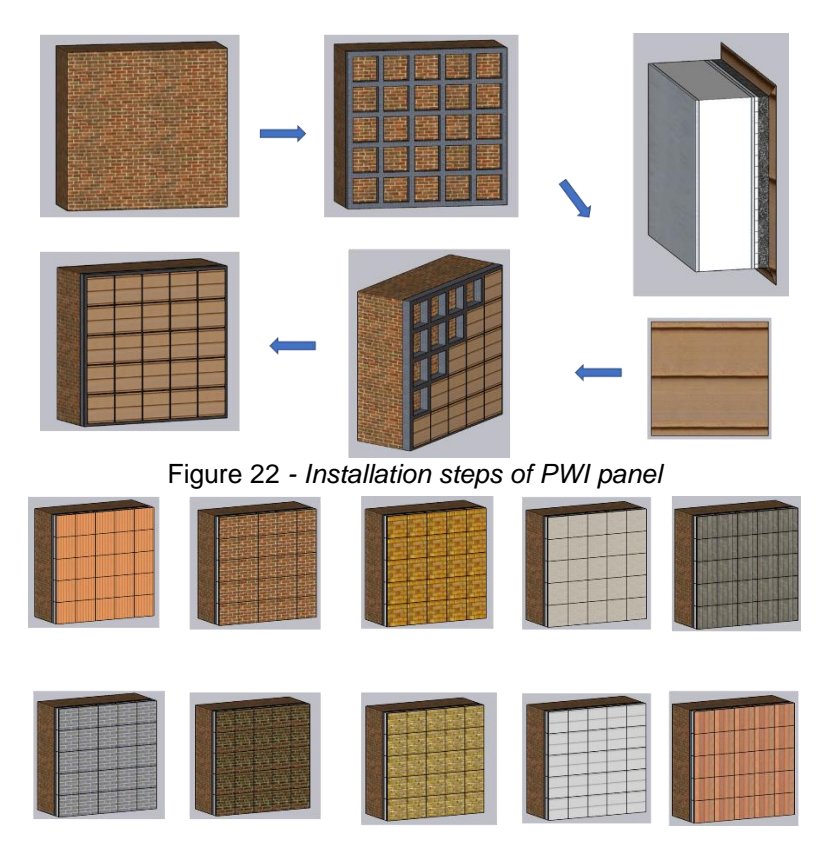


Figure 23 - Post-retrofit rendering effects

The structure of 5 PWI panels are illustrated in Figure 24, Figure 25, Figure 26, Figure 27 and Figure 28, respectively, with their axonometric and cross-sectional views displayed and each layer's material shown. In addition, the thickness, thermal conductivity and thermal resistance values are listed in Tables 5-9. Especially, the thickness and thermal resistance range from 8.2 cm to 10.6 cm and 2.986 m²K/W to 5.524 m²K/W, respectively. Furthermore, each panel has its core layer representing the insulation effect and heat transfer capability. In specific, the core layers of 5 measured PWI panels are namely Vacuum Insulation Panel (VIP) with double membrane, Starch aerogel with double membrane, silicon aerogel with double membrane, silicon aerogel with single membrane and silicon aerogel, respectively. It is observed that the core layer of Panel 5 has the lowest thermal conductivity performance, indicating that minimized heat transfer would occur through the building envelope. This means that during hot weather, less heat from the exterior penetrates the interior, reducing the need for cooling systems and decreasing energy consumption. Similarly, in cold weather, less heat escapes from the interior, resulting in reduced heating requirements. Also, silicon aerogel has high resistance to heat flow, allowing them to effectively trap and slow down the movement of thermal energy. Besides, U-value of the PWI panels is calculated with thermal resistance calculation method, which is given by Eq. (1) (Engineers March 2015):

$$U_{PWI} = (\frac{1}{h_{air,ex}} + \frac{1}{R_{PWI}} + \frac{1}{h_{air,in}})^{-1}$$
 Eq. (1)





Where, $h_{air,ex}$ is heat transfer coefficient of external air (W/m²K); $h_{air,in}$ is heat transfer coefficient of interior air (W/m²K); R_{PWI} is thermal resistance of the PWI panels (m²K/W), which is given by Eq. (2) (Engineers March 2015):

$$R_{PWI} = \frac{\delta_1}{\lambda_1} + R_{Si,1-2} + \frac{\delta_2}{\lambda_2} + R_{Si,2-3} + \dots + \frac{\delta_{n-1}}{\lambda_{n-1}} + R_{Si,n-1-n} + \frac{\delta_n}{\lambda_n}$$
 Eq. (2)

Where, δ is the thickness of each layer (m); λ is the thermal conductivity of each layer (W/mK); n is layer number for each PWI panel; R_{si} is interior surface resistance between layers (m²K/W), which is given by Eq. (3) (Engineers March 2015):

$$R_{si} = (\frac{6Eh_r}{5} + h_c)^{-1}$$
 Eq. (3)

Where, E is the emissivity factor, h_r is the radiance heat transfer coefficient (W/m²K); h_c is the convective heat transfer coefficient (W/m²K).





Figure 24 - Structure of panel 1(Left: Axonometric view; Right: Cross-sectional view)

Table 5 - Specifications of panel 1

| No.1 | Thickness (cm) | Thermal conductivity (W/mK) | R-value (m ² K/W) |
|---|----------------|-----------------------------|------------------------------|
| XPS insulation | 3 | 0.031 | 0.968 |
| Breathable membrane | 0.6 | 0.029 | 0.207 |
| VIP panel | 2.5 | 0.008 | 3.125 |
| Breathable membrane | 0.6 | 0.029 | 0.207 |
| XPS insulation | 3 | 0.031 | 0.968 |
| Fibreglass Mesh | N/A | N/A | N/A |
| Primer | 0.1 | 0.2 | 0.005 |
| Silicon coat render | 0.7 | 0.16 | 0.044 |
| Matt (made with water-dispersed siloxane) | 0.1 | 0.7 | 0.001 |
| Total | 10.6 | | 5.524 |









Figure 25 - Structure of panel 2 (Left: Axonometric view; Right: Cross-sectional view)

Table 6 - Specifications of panel 2

| No.2 | Thickness (cm) | Thermal conductivity (W/mK) | R-value (m ² K/W) |
|---|----------------|-----------------------------|------------------------------|
| XPS insulation | 3 | 0.031 | 0.968 |
| Breathable membrane | 0.6 | 0.029 | 0.207 |
| Starch aerogel | 2.5 | 0.024 | 1.042 |
| Breathable membrane | 0.6 | 0.029 | 0.207 |
| XPS insulation | 3 | 0.031 | 0.968 |
| Fibreglass Mesh | N/A | N/A | N/A |
| Primer | 0.1 | 0.2 | 0.005 |
| Silicon coat render | 0.7 | 0.16 | 0.044 |
| Matt (made with water-dispersed siloxane) | 0.1 | 0.7 | 0.001 |
| Total | 10.6 | | 3.441 |





Figure 26 - Structure of panel 3 (Left: Axonometric view; Right: Cross-sectional view)

Table 7 - Specifications of panel 3

| No.3 | Thickness (cm) | Thermal conductivity (W/mK) | R-value (m²K/W) |
|---------------------|----------------|-----------------------------|--------------------|
| XPS insulation | 3 | 0.031 | 0.968 |
| Breathable membrane | 0.6 | 0.029 | 0.207 |





| Silicon-aerogel | 1.3 | 0.013 | 1.000 |
|---|-----|-------|-------|
| Breathable membrane | 0.6 | 0.029 | 0.207 |
| XPS insulation | 3 | 0.031 | 0.968 |
| Fibreglass Mesh | N/A | N/A | N/A |
| Primer | 0.1 | 0.2 | 0.005 |
| Silicon coat render | 0.7 | 0.16 | 0.044 |
| Matt (made with water-dispersed siloxane) | 0.1 | 0.7 | 0.001 |
| Total | 9.4 | | 3.399 |



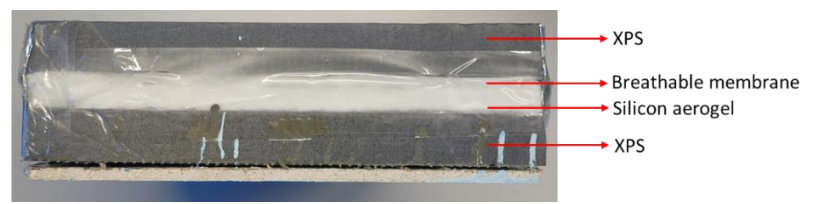


Figure 27 - Structure of panel 4 (Left: Axonometric view; Right: Cross-sectional view)
Table 8 - Specifications of panel 4

| No.4 | Thickness (cm) | Thermal conductivity (W/mK) | R-value (m²K/W) |
|---|----------------|-----------------------------|--------------------|
| XPS insulation | 3 | 0.031 | 0.968 |
| Breathable membrane | 0.6 | 0.029 | 0.207 |
| Silicon-aerogel | 1.3 | 0.013 | 1.000 |
| XPS insulation | 3 | 0.031 | 0.968 |
| Fibreglass Mesh | N/A | N/A | N/A |
| Primer | 0.1 | 0.2 | 0.005 |
| Silicon coat render | 0.7 | 0.16 | 0.044 |
| Matt (made with water-dispersed siloxane) | 0.1 | 0.7 | 0.001 |
| Total | 8.8 | | 3.193 |









Figure 28 - Structure of panel 5 (Left: Axonometric view; Right: Cross-sectional view)

Table 9 - Specifications of panel 5

| No.5 | Thickness (cm) | Thermal conductivity (W/mK) | R-value (m ² K/W) |
|---|-------------------|-----------------------------|------------------------------|
| XPS insulation | 3 | 0.031 | 0.968 |
| Silicon-aerogel | 1.3 | 0.013 | 1.000 |
| XPS insulation | 3 | 0.031 | 0.968 |
| Fibreglass Mesh | N/A | N/A | N/A |
| Primer | 0.1 | 0.2 | 0.005 |
| Silicon coat render | 0.7 | 0.16 | 0.044 |
| Matt (made with water-dispersed siloxane) | 0.1 | 0.7 | 0.001 |
| Total | 8.2 | | 2.986 |

Five PWI panel prototypes are manufactured using different insulation cores, as shown in Figures 24-28. The U-value of the prototype was evaluated using the TEC-driven calibrated hot box built at the University of Nottingham. As can be seen in Figure 29, by following closely ISO 12567 standards, the sample was installed at the specimen area of the calibrated hot box. It was tested under the standard temperature differences of 30 °C, with the cold side temperature of -5 °C and hot side temperature of 25 °C. The testing period is counted for consecutive 72 hours in steady conditions. The testing rig condition is shown in Figure 30, where the air temperature sensors are installed 10 cm away from the testing panels. Besides, 5 temperature sensors are installed on both hot and cold external surfaces of testing panels. The heat flux sensors are also adhered to the centre of the hot side surface of the panel. However, the air speed in the hot and cold side were fixed at 0.3 m/s and 1.5 m/s respectively. Using the calibrated hot box, we could estimate the total heat transfer coefficient from the hot and cold surface of the PWI prototypes. The values were then used as the input parameters for the computer simulation. To derive the absolute error, the Kline-McClintock second power law as given in NCEES (National Council of Examiners for Engineering and Surveying) (2001) is used. These errors were represented by the error bars of the associated curves. Additionally, the guideline in ISO 12567 was also being referred to evaluate the error from indoor testing.





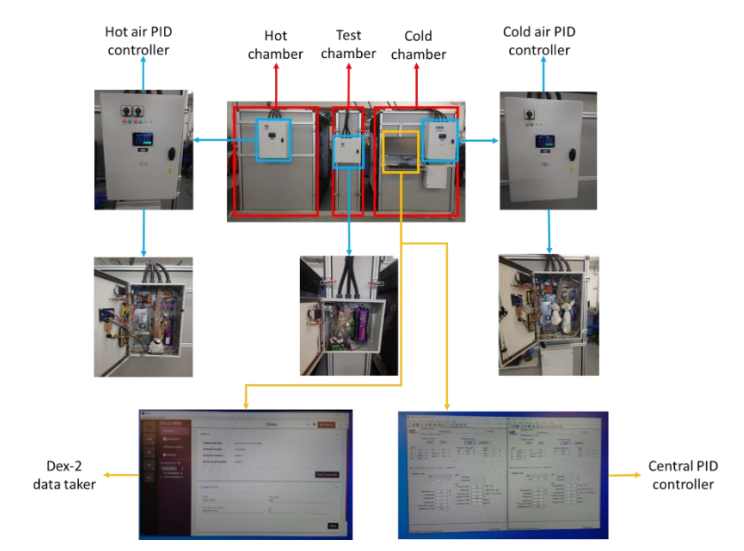


Figure 29 - The concept and structure of hot box

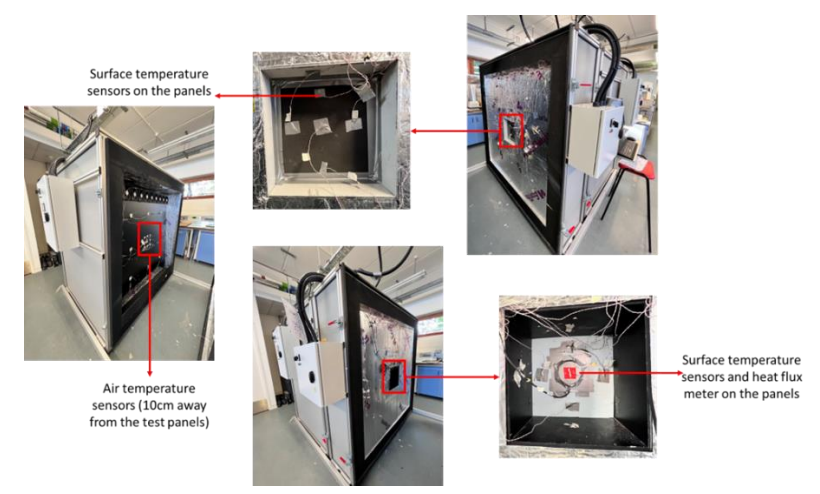


Figure 30 - The testing rig condition





4 Results and discussion

4.1 Bio-aerogel insulation panel

As shown in Figure 31, the average U-value with the starch-based aerogel insulation panel is reduced from 0.23 W/m 2 K (original wall) to 0.16 W/m 2 K, with fluctuation range floated between 0.13 W/m 2 K and 0.20 W/m 2 K. The thermal conductivity of the starch-based aerogel insulation panels is calculated as 0.024 W/mk is slightly higher than the theory value of 0.023 W/mk. However, the K-value is varied from 0.013 to 0.069 W/mk.

Besides, the internal air temperature with 100mm distance from the panel (average 30.97° C) is 1.92° C higher than that with 30mm distance (average 29.05° C). And the external ambient temperature with 100mm distance from the panel (average 3.03° C) is 0.18° C lower than that with 30mm distance (average 2.86° C).

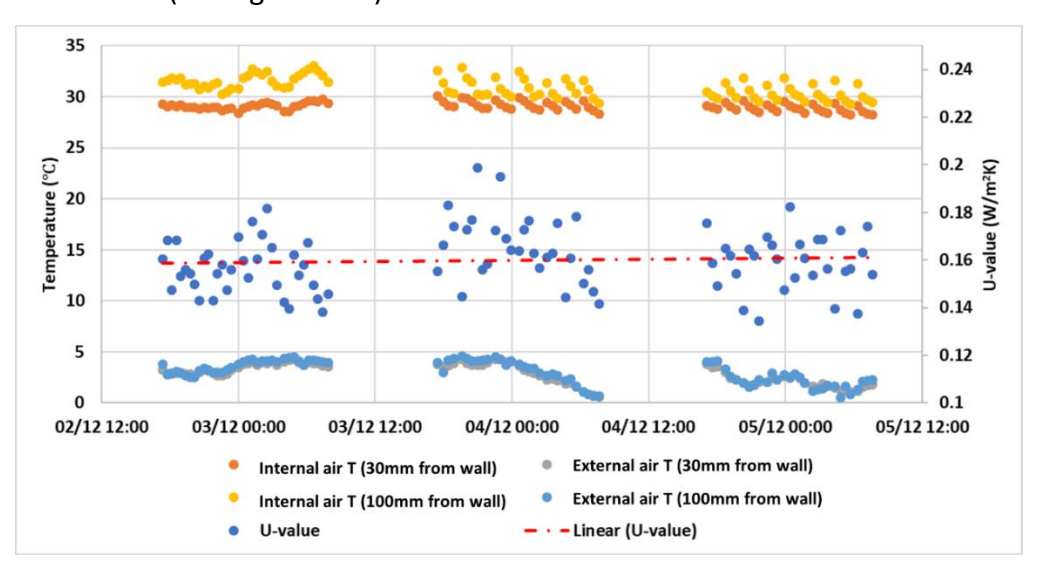


Figure 31 - U-value of interior wall with starch-based aerogel insulation panels (72 continuous nights)

Figure 32 indicates the thermal comfort improvement with starch-based aerogel insulation panels under the external ambient temperature (100mm distance) of approximately 3.0°C. It is found that the internal and external 30mm air temperature difference with insulation panel is approximately 26.19 °C, which is 4.56°C improved compared with the 30mm air temperature difference of approximately 21.63 °C without the insulation panels. Therefore, the internal insulated air temperature (30mm wall distance) increased by 1.19°C compared with the original one without insulation materials.



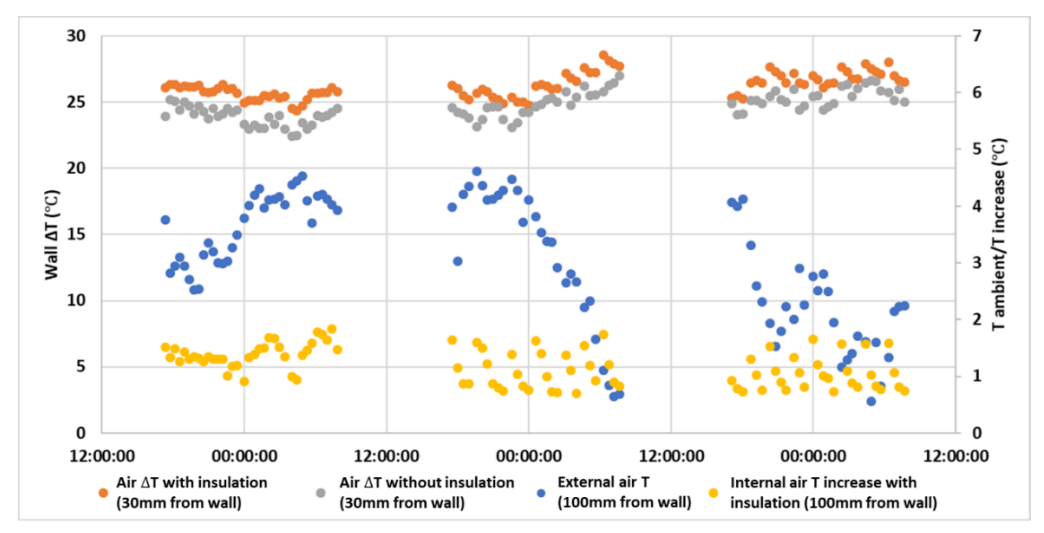


Figure 32 - Thermal comfort with starch-based aerogel based vacuum insulation panels (72 continuous nights)

4.2 PV vacuum glazing unit

In terms of efficient building sector, there is a great potential for building-integrated PV technologies (BIPV) to offer potential energy savings of a building by generating solar energy resources captured via the building materials itself. According to the electricity efficiency described in *Figure 33*, the maximum solar electricity efficiency occurred with 3.7% when solar radiation reaches approximately 520W/m2.

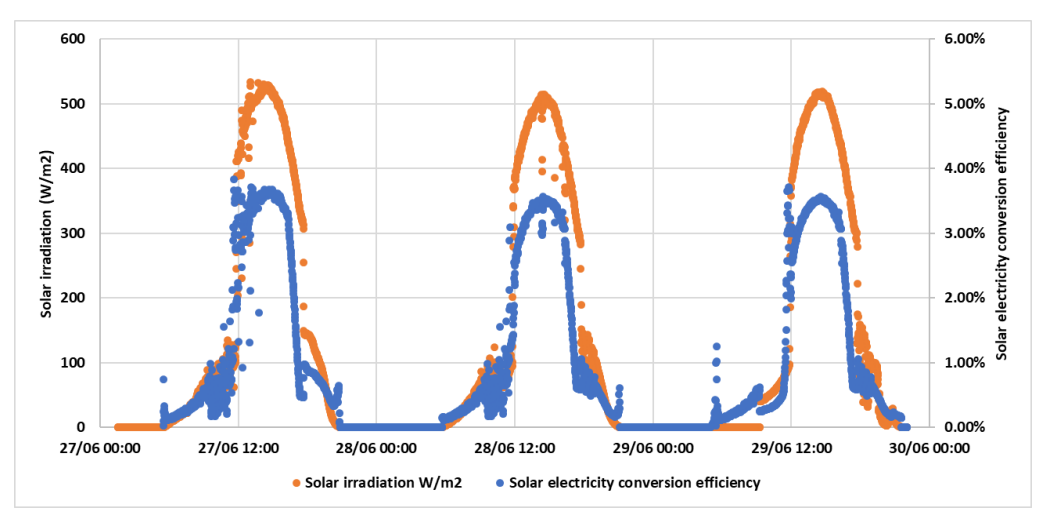


Figure 33 - Solar and electricity conversion efficiency with testing of PV VG-4L

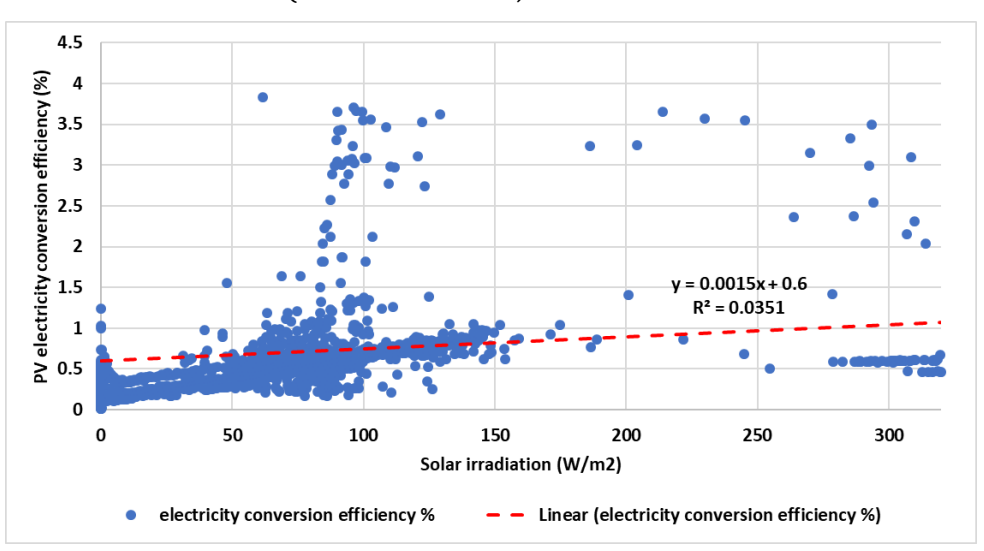
In order to clearly demonstrate the solar electricity conversion efficiency trend with the increasing of the solar radiation, the relationship between the solar radiation and the electricity conversion efficiency is concluded in *Figure 34*(a) and (b), which can furtherly be used in the future modelling with building retrofit project. Besides, it is noted that the impact of temperature change to the PV electricity conversion efficiency is not considered. In *Figure 34*(a), the average



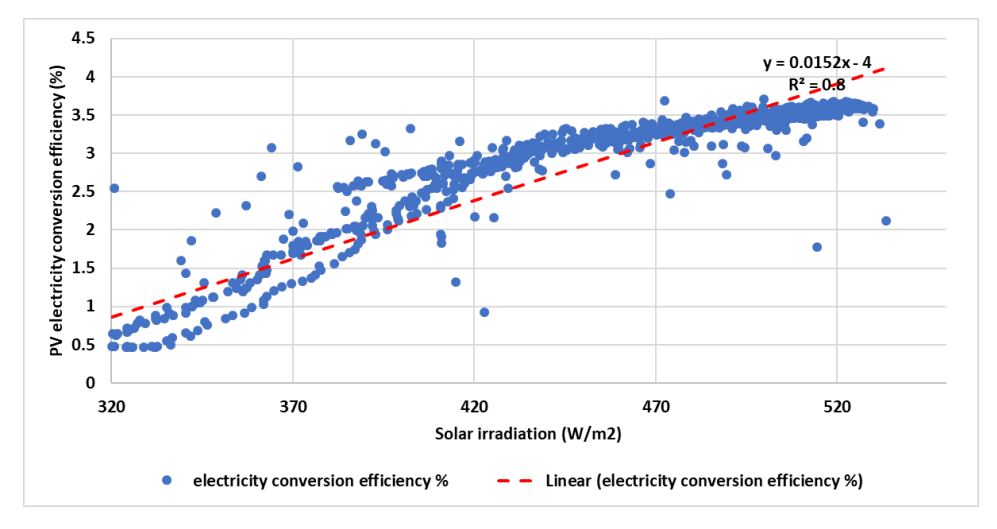


PV electricity conversion efficiency increased from 0 to 1.08% with increasing rate of 0.15% under solar radiation lower than 320W/m². However, the average PV electricity conversion efficiency increased from 1.05% to 3.90% with increasing rate of 1.52% under solar radiation varied from 320W/m² to 550W/m². Therefore, it is figured out that the PV electricity conversion efficiency increasing rate is changed from 0.15% to 1.52% with solar radiation varied between 0-320W/m² and 320-550W/m², respectively. The function of solar PV electricity conversion efficiency (f(s)) with solar radiation (s) is illustrated below:

$$f(s) = \begin{cases} 0.15\% \times s + 0.6, & 0 < s < 320 \\ 1.52\% \times s - 4.0, & 320 \le s < 550 \end{cases}$$



(a) PV electricity conversion efficiency with solar radiation below 300W/m²



(b) PV electricity conversion efficiency with solar radiation above 300W/m²

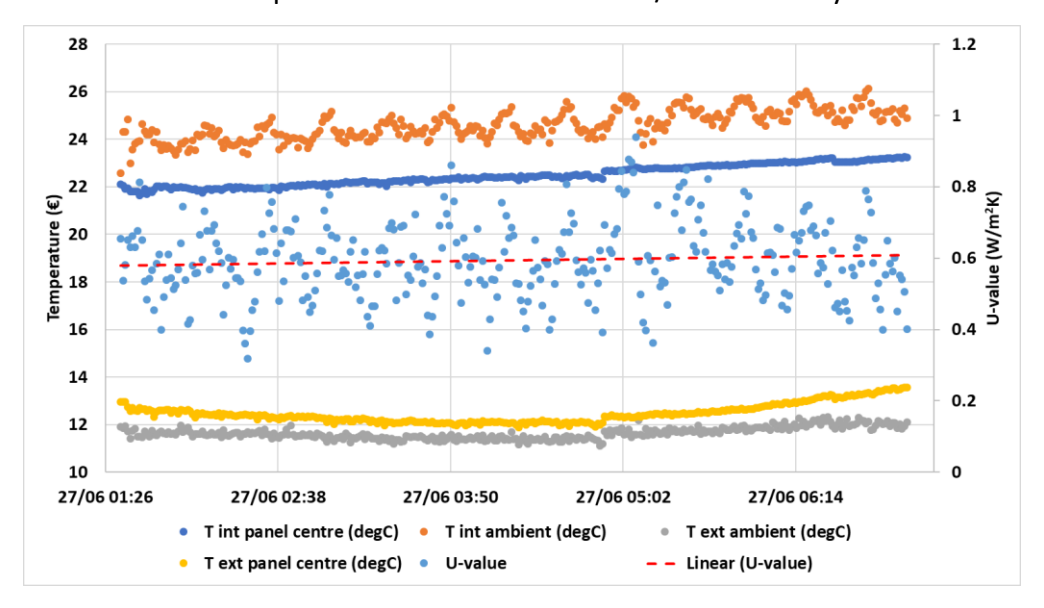
Figure 34 - PV electricity conversion efficiency with solar radiation

Figure 35 (a) (b) and (c) indicates the measured U-value with air temperature of both internal and external side. The measurement is carried out in three successive days from 27th June to 30th June in 2021. Besides, there are approximately 10°C difference between the internal and

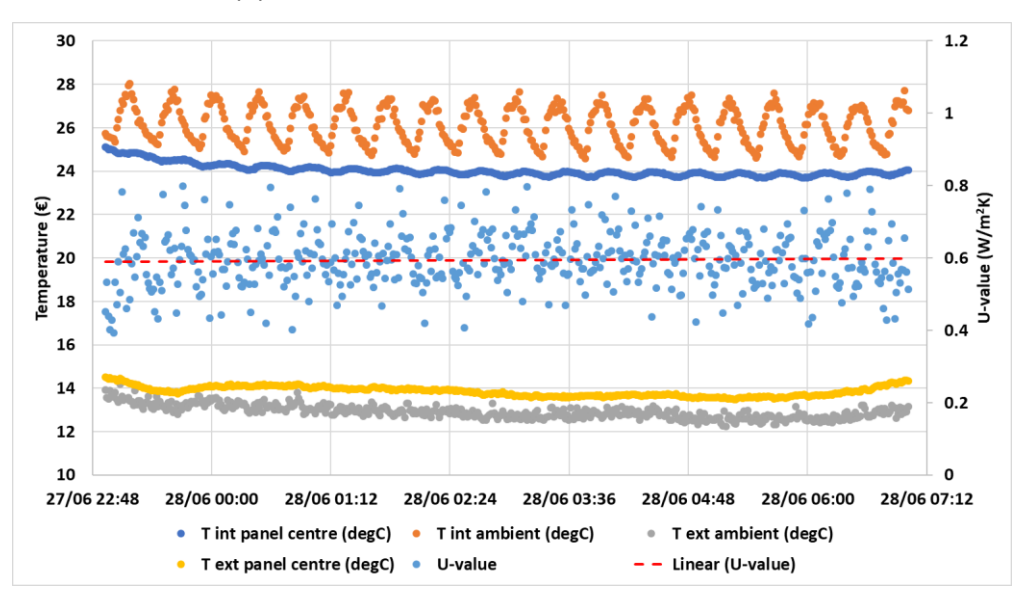
09/04/2024



external ambient air temperature. According to the heat flux and air temperature difference of internal and external sides, the U-value is calculated with an average of $0.60 \text{ W/m}^2\text{K}$, which has error difference of 5.3% compared with U-value of $0.57 \text{ W/m}^2\text{K}$ in theory.



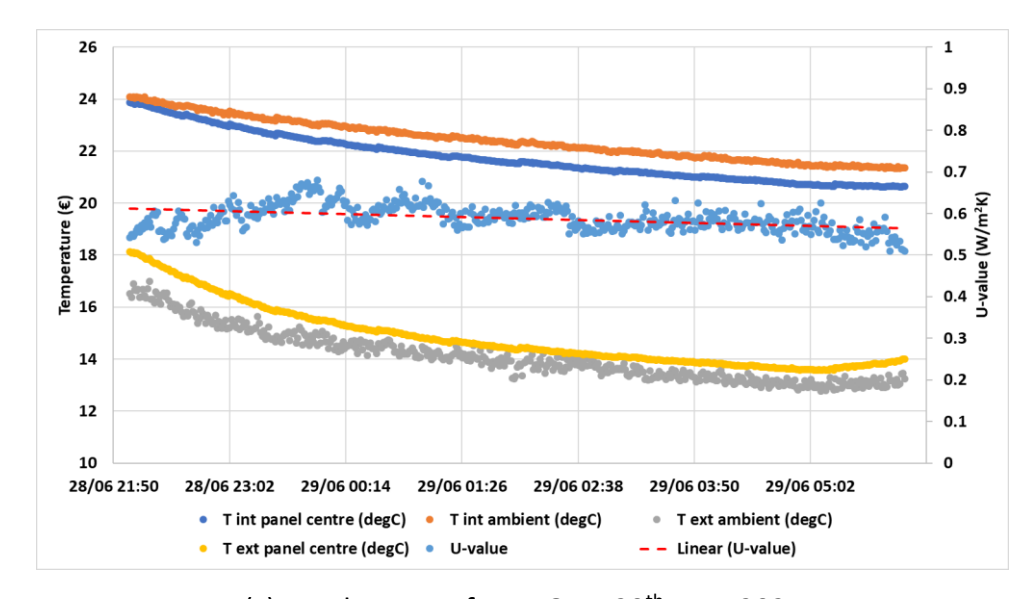
(a) U-value test of PV-VG on 27th June 2021



(b) U-value test of PV-VG on 28th June 2021







(c) U-value test of PV-VG on 29th June 2021

Figure 35 - U-value of PV VG-4L in different time periods (a) (b) (c)

4.3 PCM panel

The initial testing showed that S27 was the most efficient PCM to use in our application and therefore this was selected for testing moving forward, as shown in Figure 36.

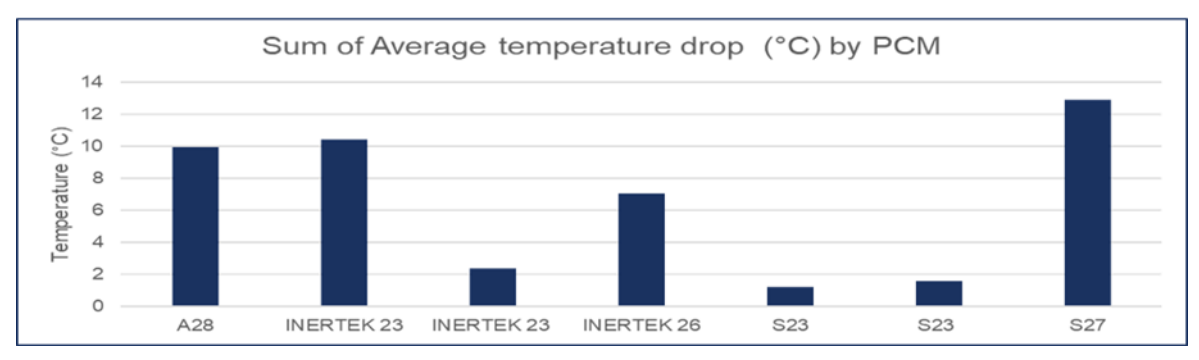


Figure 36 - Test results

Blister panels were identified as better option than pouches due to Increased heat transfer area and less prone to damage. A manufacturer was identified and instructed to produce prototypes using S27 PCM material, as shown in *Figure 37*.





09/04/2024





Figure 37 - Blister PCM Panel prototype

The blister panel design was found problematic for filling, robustness and cost effectiveness therefore a cheaper and more robust prototype, a HDPE encapsulated panel (*Figure 38*) was developed and manufactured by PCM Products.



Figure 38 - Thin Ice Panel

38 Panels with S27 PCM were supplied to University of Nottingham for laboratory scale testing.

A set of 14 PCM panels were allocated in the SRB room in UoN with a total weight of 49.81kg, 3.55kg each, as shown in *Figure 39*. The testing room has a total area of 5.49 m^2 and each panel measures 49 x 24 cm. The area covered by the PCM panel corresponds to 1.4 m^2 representing 25% of the area. The panels were tested under different conditions to determine the impact on the room. The measurements were taken with a Data logger and 5 thermocouples.

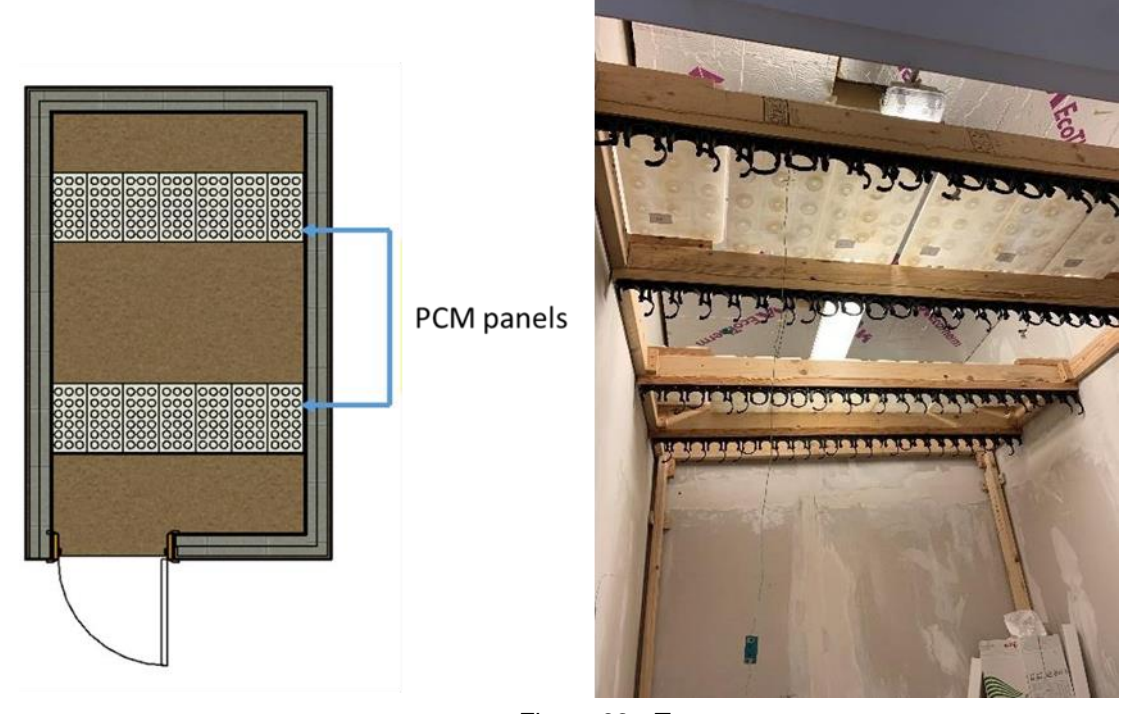


Figure 39 - Test room

The radiator was used to preheat the room for 24hrs before testing, after this period the radiator was turned off, with room temperature shown in *Figure 40*.





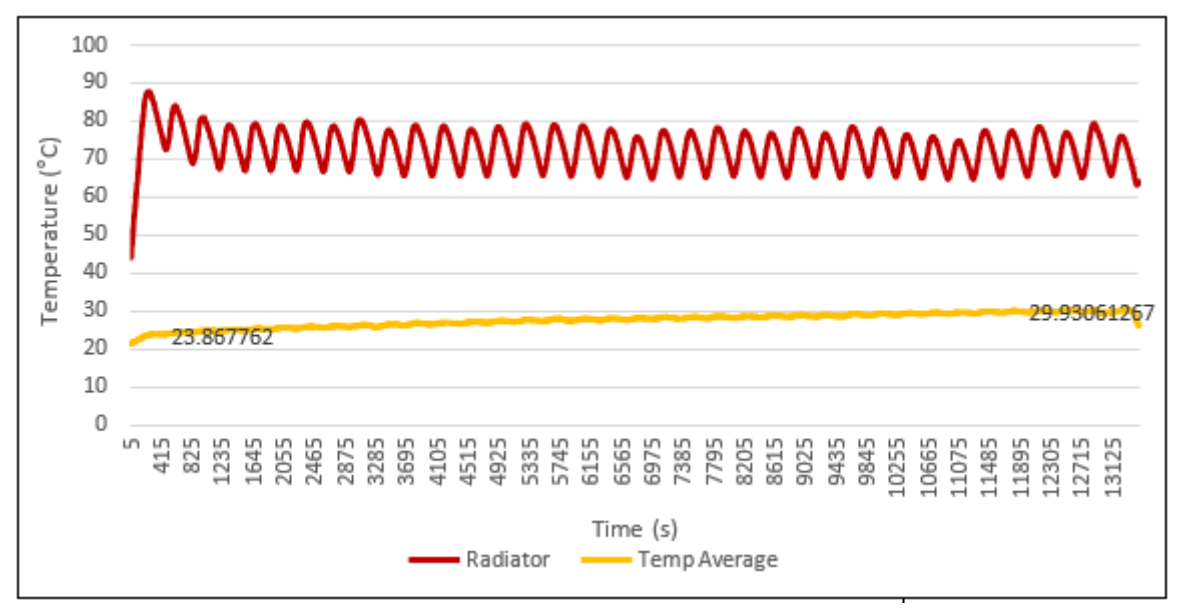


Figure 40 - Room temperature without PCM and Radiator for heating

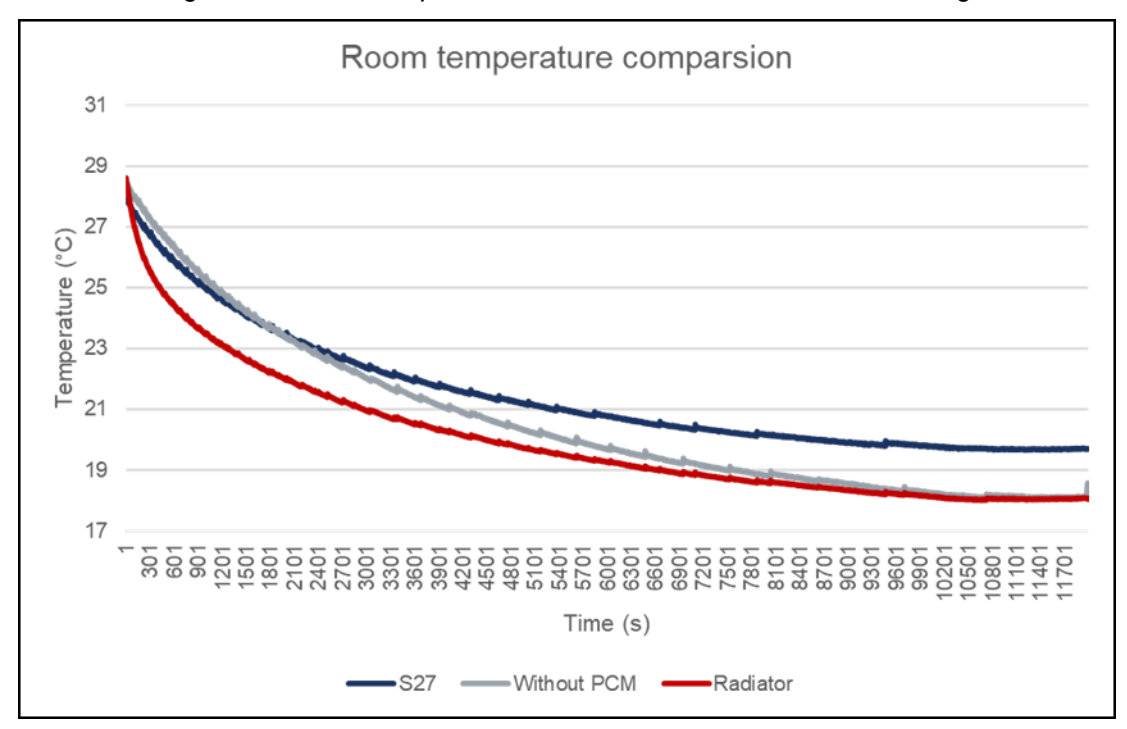


Figure 41 - Room temperature comparison

It was observed that the S27 was able to maintain higher temperatures, whereas the room without PCM presents a 1.7°C temperature decrement, with room temperature shown in *Figure 41*.





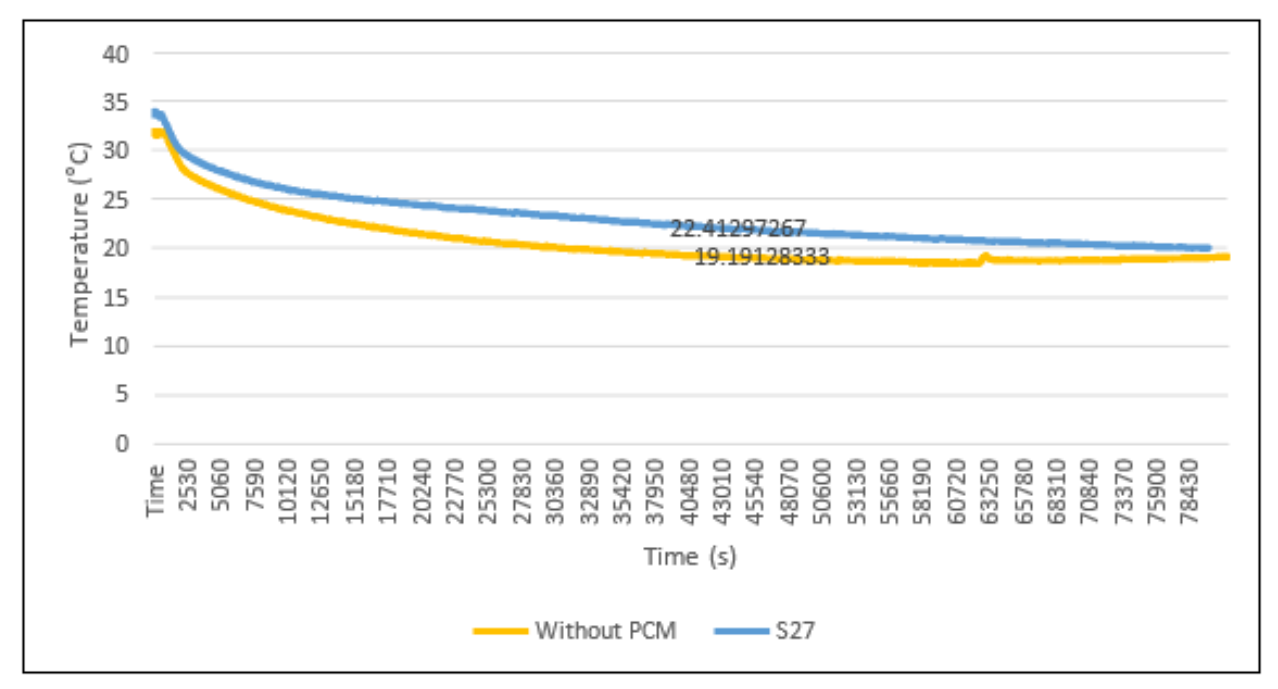


Figure 42 - Room pre heated and then heating turned off for duration of test

A second test was conducted. It is observed a maximum temperature difference of 3.3°C after 11.2 hrs. The test was repeated with two radiators to increase the room temperature, in this case the panel temperature is 26.9°C when the room temperature is of 38.33°C, with the temperature distribution shown in *Figure 42*.

4.4 Solar assisted heat pump

Figure 43 summarized the testing results of the SAHP system COP under variation of solar radiation from 0-700W/m², wind velocity from 0-2m/s, supply both the DHW and space heating.

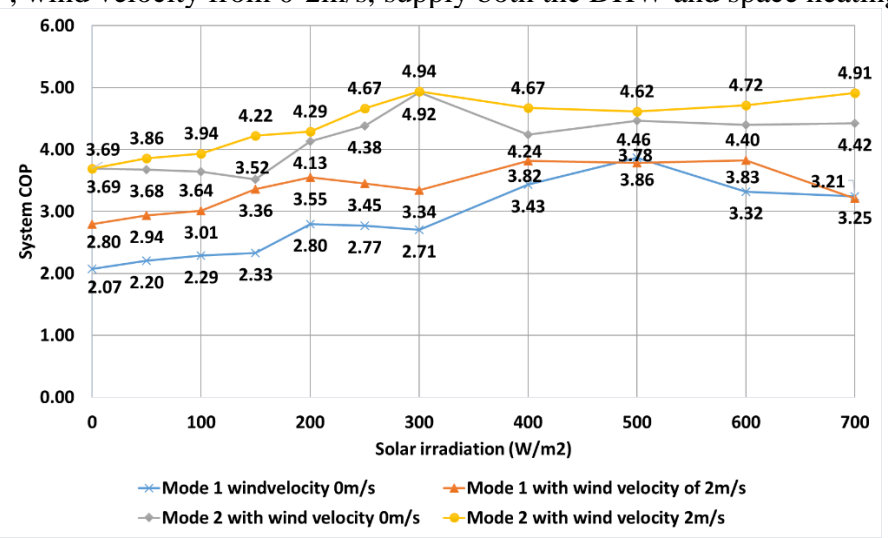


Figure 43 - Summary of system COP

Solar radiation (G_t) , environment temperature near the solar panel (T'_a) and wind speed (V) are combined in a single parameter and then used to describe the COP_H . This parameter is the plate temperature of the solar thermodynamic panel (T_p) , which is presented as below:





$$\begin{split} Q_{C} &= A \left[\eta_{0} G_{t} - U \big(T_{p} - {T'}_{a} \big) \right] \\ T_{p} &= (1 - F_{R}) \left[{T'}_{a} + \frac{\eta_{0} G_{t}}{5.7 + 3.8 V} \right] + F_{R} T_{3} \end{split}$$

Figure 44 presents the COP_H as function of T_p and the respective linear correlated equations for the four pilots. The mean squared error (R2) of the linear regressions are 0.946, 0.956, 0.973 and 0.920, respectively for UK, Greece, Portugal, and Spain.

The general \overline{COP}_H correlation, which is the mean of the four correlations, as shown below:

$$\overline{COP}_H = 0.069T_p + 2.825$$

This correlation can be used to obtain the performance of the solar assisted heat pump for different climate conditions (solar radiation, environment temperature and wind speed).

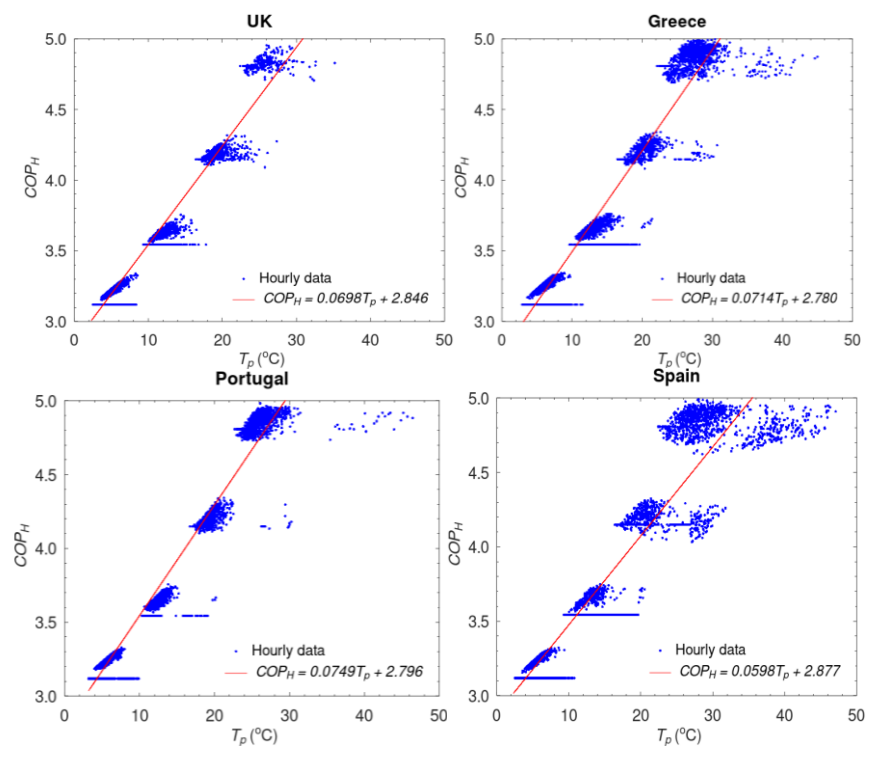


Figure 44 - Linear regression of COP_H as function of T_p for the four different pilots.

The energyPRO software is used to simulate the integrated PV-SAHP-TS system energy flow from energy source to energy demand via the integrated system, as shown in *Figure 45*. The energyPRO is the leading software for modelling and analysing complex energy projects with combined supply of electricity and thermal energy (process heat, hot water and cooling), which is used for detailed technical of both existing and new energy projects in a very user-friendly interface providing the user with a clear overview of the project. The software offers a long range of technical and economic reports including graphical presentation of the simulated operation which provides an overview and in-depth understanding of the dynamics in a complex energy system.



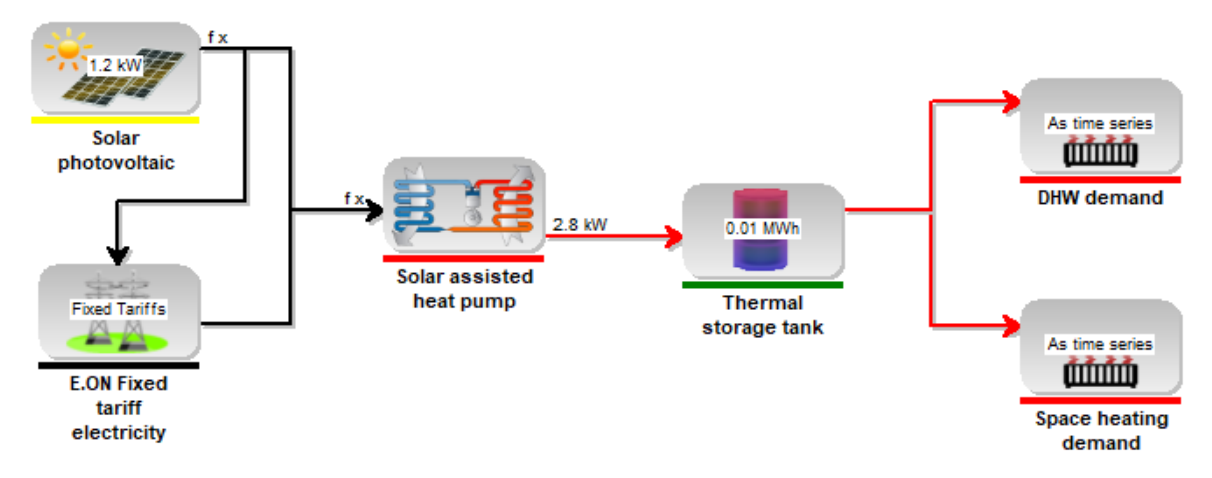


Figure 45 - Energy flow work simulation process in energyPRO software

DHW and space heating demands of the selected four pilot buildings are simulated from the ICE-IDA with results summarized in Table x. The required SAHP heating capacity is sized in the EnergyPro simulation software, which differs from the sole SAHP and PV-SAHP-TS integrated systems, as shown in *Table 10* and *Table 11*. It is noticeable that the SAHP sizes are reduced evidently in the PV-SAHP-TS integrated system with 4.1 - 5.6 kW compared with the other one with 7 – 26 kW, resulting from that the peak heating demand of the SAHP system is mitigated by the discharge process of the thermal storage tank. Besides, the SAHP system is 100% operated during efficient solar radiation period in the integrated system. Moreover, the imported electricity from the grid is significantly reduced by 27%, 50%, 57% and 61% in the integrated system of UK, Greece, Portugal and Spain pilot buildings accordingly, due to the increasing PV electricity generation.

The heating COP is increased sharply in the integrated system due to the reduced electricity consumption of the whole system. As illustrated in *Figure 46*, the annual heating COP of the sole SAHP system remains at an almost constant value ranging from 3.4 to 3.6, independent of the ambient climate context. However, it is increased by 72%, 100%, 135% and 156% of the four pilot buildings accordingly with the range from 6.2 to 9.2.

Table 10 -Building heating demand and imported electricity with sole SAHP system

| Pilot location | DHW heating demand | Space heating demand | Annual heating demand | Required SAHP heating capacity | Imported electricity from the grid |
|-------------------|--------------------------|----------------------------|-----------------------------|--------------------------------------|--|
| UK | 4.5MWh | 5.9MWh | 10.4MWh | 11kW | 8.1MWh |
| Greece | 2.8MWh | 1.4MWh | 4.2MWh | 20kW | 1.2MWh |
| Portugal | 1.2MWh | 1.2MWh | 2.4MWh | 7kW | 0.7MWh |
| Spain | 3.2MWh | 6.9MWh | 10.1MWh | 26kW | 2.8MWh |





Table 11 - Building heating demand and imported/exported electricity with PV-SAHP-TS system

| Pilot location | Annual heating demand | Required SAHP heating capacity | Hot water storage tank | Solar peak power | Imported electricity from the grid | PV exported electricity |
|-------------------|-----------------------------|---|---------------------------------|------------------------|------------------------------------|-------------------------|
| UK | 10.4MWh | 6kW | 800L | 4.1kW | 5.9MWh | 2.9MWh |
| Greece | 4.2MWh | 5kW | 400L | 5.6kW | 0.6MWh | 8.9MWh |
| Portugal | 2.4MWh | 2.8kW | 200L | 5.6kW | 0.3MWh | 9.2MWh |
| Spain | 10.1MWh | 7kW | 800L | 5.2kW | 1.1MWh | 8.1MWh |

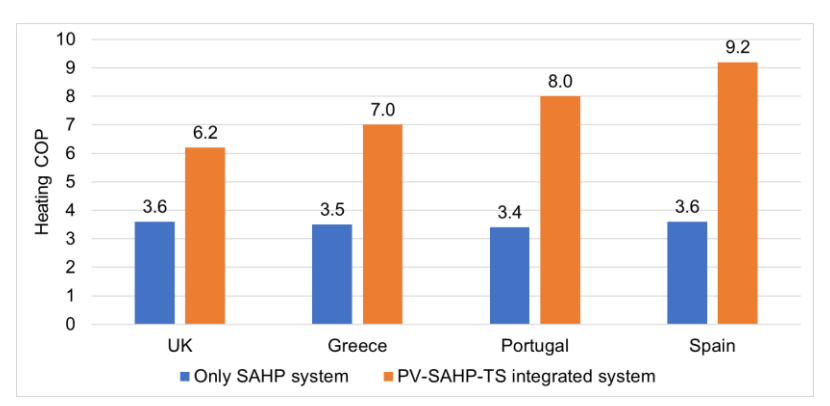


Figure 46 - Heating COP of sole SAHP and PV-SAHP-TS integrated systems

4.5 Ground source heat pump

The Figure 47 shows the averaged results for each moisture factor. There is a clear and obvious trend that increased moisture factors lead to increased thermal conductivity. This would suggest that if electroosmotic flow can be implemented in the Efficient Geotech solution, there are significant heat transfer benefits which could be obtained.

The cross marks show the thermal conductivity of the enhanced soils. It suggests that clay soils have the most to gain from being enhanced, with a thermal conductivity improvement of +0.88 W/mK (+93%). There were improvements in all types of soils tested.





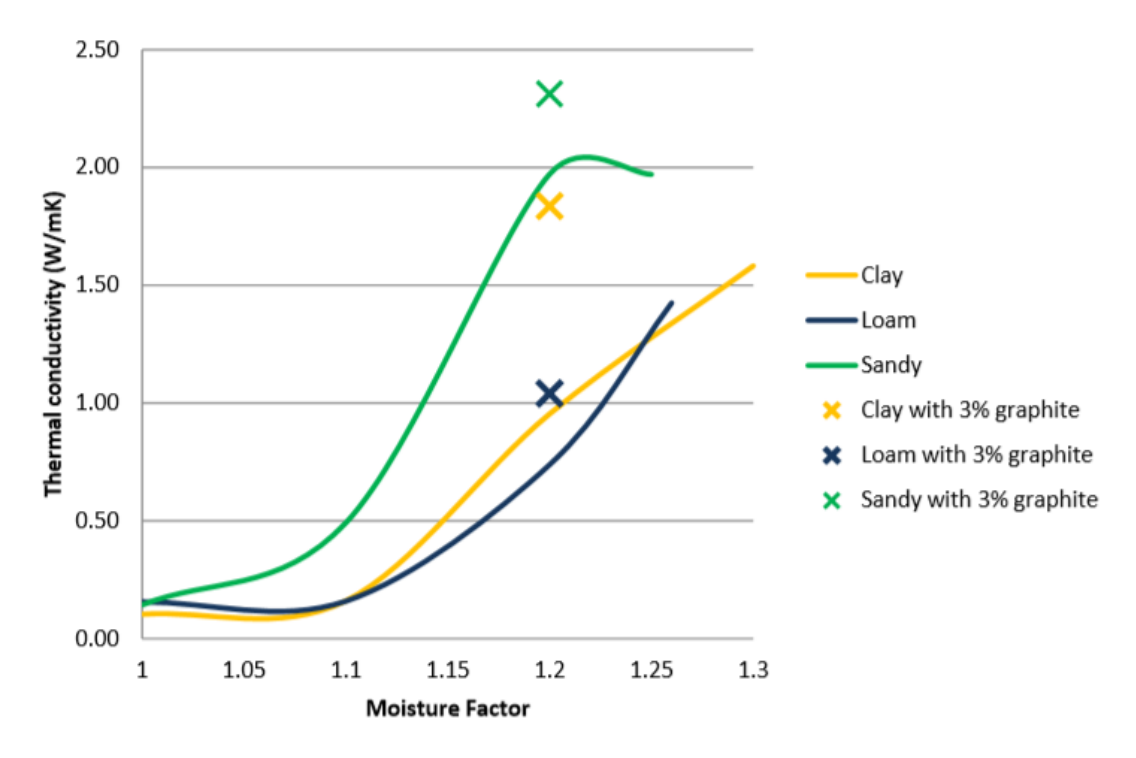


Figure 47 - averaged results for each moisture factor

Besides, tests were also conducted with 3kW and 6kW heating capacity under rated heating output at B0/W35 and B0/W55 with BS EN14511 testing standards. Besides, the Brine temperature is based on 0° C in / -4° C out. The energy performance is shown in *Table 12*.

Table 12 - Energy performance results of 3kW and 6kW heating capacity

| Thermal heating capacity | 3.0kW | 6.0kW |
|--|-------|-------|
| Performance data - rated heating output at B0/W35 BS EN14511 | | |
| Power consumption | 0.8kW | 1.6kW |
| Co-efficient of Performance | 4.05 | 3.84 |
| Design flow rate kg/min | 9.2 | 18.4 |
| Pressure drop kPa at design flow rate | 5 | 16 |

Heating water based on 30°C in / 35°C out





| Design flow rate I/min | 8.62 | 16.88 |
|---|------|-------|
| Pressure drop kPa at design flow rate | 1.0 | 0.64 |
| Max flow temperature °C | 65 | 65 |
| Heating water based on 30°C in / 55°C out | | |
| Co-efficient of Performance | 2.99 | 2.97 |
| Seasonal space heating energy efficiency | 112% | 111% |

4.6 Evaporative cooling unit

For validation, the model is adjusted to the same experimental condition and the measurements and numerical results are compared. The measured and modelled air outlet temperature and relative humidity were compared for three different inlet air mass flow rates, which are: $\dot{m}_a = 57 \text{ m}^3/\text{h}$, $114 \text{ m}^3/\text{h}$ and $171 \text{ m}^3/\text{h}$. The solution mass flow rate was fixed to 2 litters per minute with a concentration of 40%. *Table 13* to *Table 15* present the comparison between experimental and numerical for different inlet temperature of solution $T_{s,in}$ and different inlet temperature $T_{a,in}$ and relative humidity of $RH_{a,in}$ air.

Table 13 - Comparison between measurements and numerical for $\dot{m}_a = 57~\text{m}^3/\text{h}$.

| Inle | et conditi | ons | Ex | kperimen | tal | | Numeric | al | | Error (% | 6) |
|-----------------|-----------------|-----------------|------------------|----------------------|-----------------------------|------------------|----------------------|-----------------------------|-----------------|-------------------|-------------------------|
| $T_{s,in}$ (°C) | $T_{a,in}$ (°C) | $RH_{a,in}$ (%) | $T_{s,out}$ (°C) | $ar{T}_{a,out}$ (°C) | $\overline{RH}_{a,out}$ (%) | $T_{s,out}$ (°C) | $ar{T}_{a,out}$ (°C) | $\overline{RH}_{a,out}$ (%) | $ar{T}_{s,out}$ | $\bar{T}_{a,out}$ | $\overline{RH}_{a,out}$ |
| 23.2 | 29.8 | 72.8 | 25.0 | 27.9 | 72.3 | 25.6 | 27.6 | 67.5 | 2.5 | 1.2 | 6.6 |
| 21.3 | 29.4 | 73.0 | 23.3 | 26.0 | 70.7 | 24.2 | 26.7 | 66.4 | 3.9 | 2.5 | 6.1 |
| 17.4 | 29.3 | 73.6 | 20.0 | 25.3 | 67.3 | 21.5 | 25.2 | 64.2 | 7.4 | 0.3 | 4.5 |
| 17.6 | 29.3 | 72.3 | 22.4 | 25.0 | 63.6 | 21.5 | 25.3 | 63.8 | 3.9 | 1.1 | 0.3 |
| 14.2 | 29.4 | 74.1 | 19.5 | 25.0 | 66.5 | 19.2 | 24.2 | 62.9 | 1.3 | 3.4 | 5.5 |
| 16.9 | 29.4 | 72.1 | 22.3 | 25.3 | 63.8 | 21.0 | 25.1 | 63.3 | 5.6 | 0.7 | 0.9 |
| 15.0 | 29.4 | 72.3 | 21.4 | 24.5 | 62.0 | 19.7 | 24.4 | 62.4 | 8.0 | 0.4 | 0.7 |
| 12.7 | 29.4 | 74.8 | 19.5 | 24.4 | 64.2 | 18.2 | 23.6 | 62.6 | 6.8 | 3.3 | 2.5 |





| 9.2 | 29.4 | 74.9 | 16.5 | 23.7 | 59.9 | 15.5 | 22.4 | 61.7 | 6.0 | 5.8 | 3.0 |
|------|------|------|------|------|------|------|------|------|------|-----|-----|
| 13.6 | 29.3 | 73.2 | 22.0 | 23.9 | 65.0 | 18.7 | 23.9 | 62.2 | 15.1 | 0.2 | 4.2 |

Table 14 - Comparison between measurements and numerical for $\dot{m}_a=114~\text{m}^3/\text{h}.$

| In | let condit | ions | E | xperimen | tal | | Numerica | I | | Error (% | 5) |
|-----------------|-----------------|---------------------------|------------------|----------------------|-----------------------------|-------------------------|----------------------|-----------------------------|-------------------|-------------------|-------------------------|
| $T_{s,in}$ (°C) | $T_{a,in}$ (°C) | RH _{a,in} (%) | $T_{s,out}$ (°C) | $ar{T}_{a,out}$ (°C) | $\overline{RH}_{a,out}$ (%) | T _{s,out} (°C) | $ar{T}_{a,out}$ (°C) | $\overline{RH}_{a,out}$ (%) | $\bar{T}_{s,out}$ | $\bar{T}_{a,out}$ | $\overline{RH}_{a,out}$ |
| 20.9 | 29.8 | 72.5 | 23.3 | 27.4 | 71.5 | 24.9 | 27.9 | 68.7 | 7.0 | 1.8 | 3.9 |
| 23.8 | 29.4 | 72.5 | 27.6 | 27.9 | 70.1 | 26.4 | 28.2 | 70.0 | 4.5 | 1.0 | 0.2 |
| 18.9 | 29.3 | 71.1 | 23.4 | 27.9 | 66.3 | 23.3 | 27.0 | 67.2 | 0.4 | 3.1 | 1.4 |
| 14.6 | 29.2 | 72.7 | 20.4 | 27.2 | 69.7 | 20.7 | 26.0 | 67.3 | 1.6 | 4.5 | 3.5 |
| 15.0 | 29.3 | 71.9 | 20.9 | 27.5 | 69.3 | 21.0 | 26.1 | 66.8 | 0.2 | 5.1 | 3.6 |
| 19.6 | 29.5 | 71.5 | 26.1 | 27.5 | 68.6 | 23.9 | 27.3 | 67.7 | 8.5 | 0.6 | 1.4 |
| 20.3 | 29.4 | 71.0 | 26.8 | 27.2 | 69.7 | 24.2 | 27.4 | 67.6 | 9.7 | 0.7 | 3.0 |
| 19.4 | 29.4 | 70.9 | 26.0 | 27.5 | 68.7 | 23.6 | 27.2 | 67.3 | 9.1 | 1.1 | 2.1 |
| 14.0 | 29.2 | 72.3 | 20.7 | 26.9 | 68.8 | 20.3 | 25.8 | 66.9 | 2.0 | 4.0 | 2.7 |
| 13.0 | 29.1 | 74.0 | 19.9 | 26.9 | 69.6 | 19.8 | 25.5 | 67.9 | 0.7 | 5.2 | 2.5 |
| 17.5 | 29.4 | 70.7 | 24.4 | 26.7 | 67.2 | 22.5 | 26.8 | 66.6 | 7.9 | 0.4 | 0.9 |
| 19.4 | 29.5 | 71.2 | 26.3 | 27.1 | 68.9 | 23.7 | 27.3 | 67.4 | 9.8 | 0.7 | 2.1 |
| 9.3 | 29.4 | 71.3 | 16.8 | 26.2 | 66.8 | 17.1 | 24.8 | 65.9 | 1.8 | 5.0 | 1.3 |
| 18.5 | 29.5 | 71.9 | 26.4 | 27.3 | 69.2 | 23.3 | 27.1 | 67.6 | 11.9 | 0.7 | 2.3 |
| 13.0 | 29.4 | 73.0 | 21.0 | 25.5 | 66.1 | 19.8 | 25.7 | 67.2 | 5.6 | 0.9 | 1.8 |
| 14.4 | 29.2 | 71.6 | 22.6 | 25.9 | 67.1 | 20.5 | 25.9 | 66.5 | 9.4 | 0.0 | 0.9 |
| 15.2 | 29.2 | 71.7 | 23.7 | 26.6 | 70.0 | 21.0 | 26.1 | 66.7 | 11.4 | 2.0 | 4.6 |

Table 15 - Comparison between measurements and numerical for \dot{m}_a = 171 $\text{m}^3\text{/h}.$

| Inle | Inlet conditions Experimental | | tal | Numerical | | | | Error (%) | | | |
|-----------------|-------------------------------|---------------------------|------------------|-------------------------------|-----------------------------|------------------|-------------------------------|-----------------------------|-----------------|------------------------|-------------------------|
| $T_{s,in}$ (°C) | $T_{a,in}$ (°C) | RH _{a,in} (%) | $T_{s,out}$ (°C) | $ar{\mathit{T}}_{a,out}$ (°C) | $\overline{RH}_{a,out}$ (%) | $T_{s,out}$ (°C) | $ar{\mathit{T}}_{a,out}$ (°C) | $\overline{RH}_{a,out}$ (%) | $ar{T}_{s,out}$ | $\overline{T}_{a,out}$ | $\overline{RH}_{a,out}$ |





| 22.8 | 30.2 | 71.7 | 26.2 | 28.8 | 71.2 | 26.5 | 29.0 | 69.8 | 1.1 | 0.8 | 2.0 |
|------|------|------|------|------|------|------|------|------|-----|-----|-----|
| 17.3 | 29.9 | 69.2 | 22.5 | | 71.5 | 23.0 | 27.8 | 66.9 | 2.3 | 1.5 | 6.4 |
| | | | | | | | | | | | - |
| 16.9 | 30.1 | 72.2 | 22.8 | 27.9 | 70.7 | 23.3 | 27.9 | 69.1 | 2.1 | 0.2 | 2.3 |
| 17.7 | 31.0 | 71.4 | 23.7 | 28.0 | 71.3 | 24.2 | 28.8 | 68.5 | 2.1 | 2.9 | 3.8 |
| 16.5 | 30.2 | 71.4 | 23.3 | 27.7 | 68.9 | 23.0 | 27.9 | 68.4 | 1.3 | 0.9 | 0.6 |
| 14.7 | 29.9 | 70.0 | 21.6 | 26.9 | 71.2 | 21.6 | 27.3 | 67.2 | 0.1 | 1.5 | 5.6 |
| 13.5 | 29.9 | 70.2 | 21.4 | 27.0 | 70.8 | 20.9 | 27.1 | 67.3 | 2.4 | 0.6 | 4.8 |
| 11.2 | 30.3 | 70.6 | 19.3 | 27.1 | 69.3 | 19.7 | 27.1 | 67.6 | 2.3 | 0.2 | 2.4 |
| 12.9 | 31.0 | 69.9 | 21.3 | 26.8 | 69.7 | 21.2 | 27.9 | 67.1 | 0.7 | 4.1 | 3.8 |
| 12.1 | 30.0 | 70.4 | 21.7 | 27.0 | 69.8 | 20.1 | 27.0 | 67.5 | 7.4 | 0.2 | 3.4 |

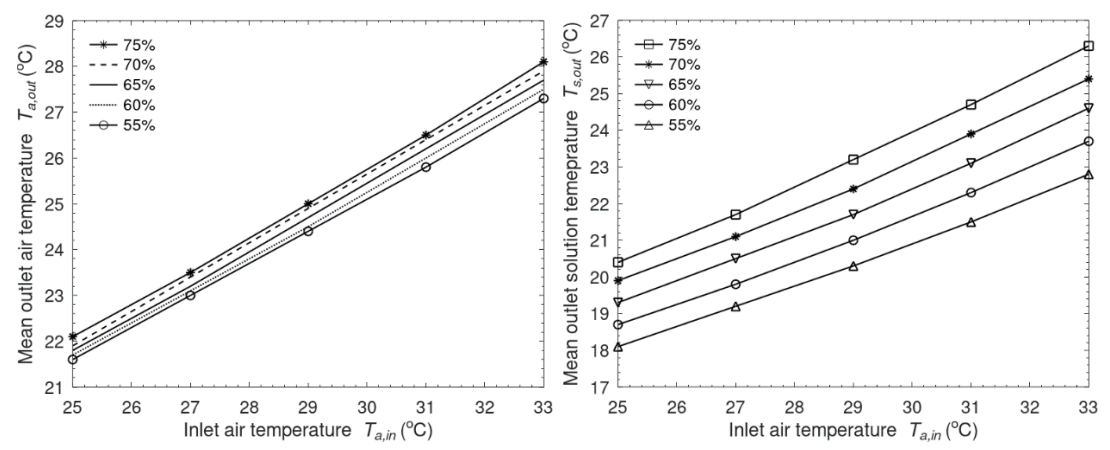


Figure 48 - Effect of inlet air temperature on outlet air humidity and solution temperature

It is figured out from Figure 48 that both air and solution mean outlet temperatures increase with the increment of the inlet air temperature under different humidity ranging from 55% to 75%. However, the growth rate is relatively rapid for solution mean outlet temperature with the increasing humidity than that of airside. For the air mean outlet temperature at five different humidity, the minimum and maximum temperature differences are 0.5 °C and 0.8 °C , respectively. For the solution mean outlet temperature at five different humidity, the minimum and maximum temperature differences are 1.7° C and 3.5° C, respectively.



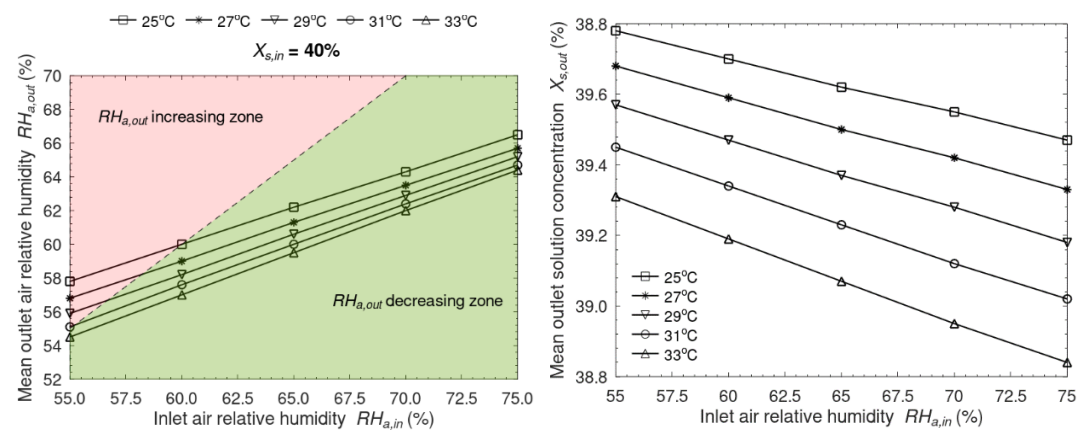


Figure 49 - Effect of inlet air relative humidity on outlet air humidity and solution concentration

As depicted in *Figure 49*, two distinctive zones of mean air outlet relative humidity (increasing and decreasing zones) are determined within which $RH_{a,in}$ equals $RH_{a,out}$ at 60% of inlet air humidity level. In the increasing zone, the inlet air humidity is less than that of the outlet humidity, and vice versa in the decreasing zone (i.e., $RH_{a,in}$ =55%, $RH_{a,out}$ =58%). Moreover, the inlet air relative humidity is proportional to its outlet humidity with the air temperature rise. Nonetheless, the relationship between inlet air relative humidity and mean outlet solution concentration shows dissimilarities where the mean outlet solution concentration air inlet humidity declines with the inlet humidity rise, with minimum and maximum concentration differences of 0.47% and 0.63%, respectively.

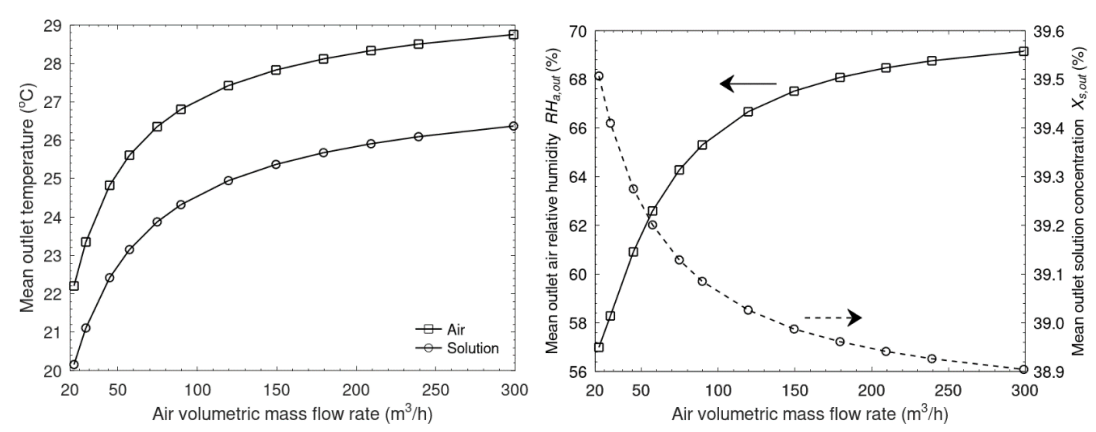


Figure 50 - Effect of air mass flow rate on outlet air temperature/humidity and solution concentration

It is discovered from *Figure 50* that both air and solution mean outlet temperatures escalate with the increasing air mass flow rate at 40% concentration indicating a higher cooling capacity, where the minimum and maximum temperature differences between air and solution are 2.05°C and 2.38°C, respectively. Specifically, the outlet temperature increases speedily with a relatively smaller air mass flow rate, whereas increasing steadily with a larger value. Unlike the variation trend of outlet temperature, the solution outlet humidity decreases with the increasing air mass flow rate causing a comparable concentration decline, while outlet humidity at the airside ascends with the air mass flow rate, which is an unacceptable and unreasonable scenario. Therefore, an optimised air mass flow rate has been found as 57m³/h to cope with the issue.



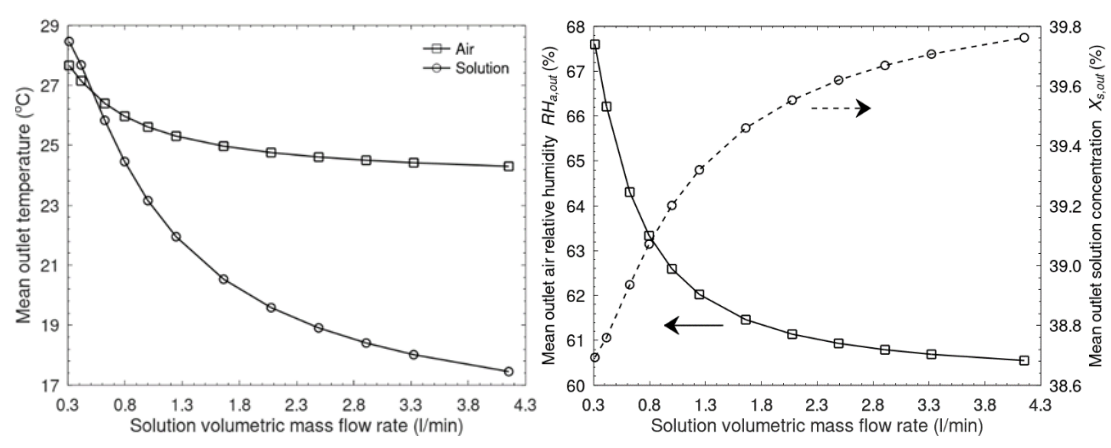


Figure 51 - Effect of solution mass flow rate on outlet air temperature/humidity and solution concentration

It is discovered from *Figure 51* that both air and solution mean outlet temperatures decline with increasing solution mass flow rate at 40% concentration, where the minimum and maximum temperature differences between air and solution are 0.53°C and 6.85°C, respectively. Likewise, the air outlet humidity decreases with the increasing solution mass flow rate causing the concentration reduction. In addition, the optimised solution mass flow is 1 l/min.

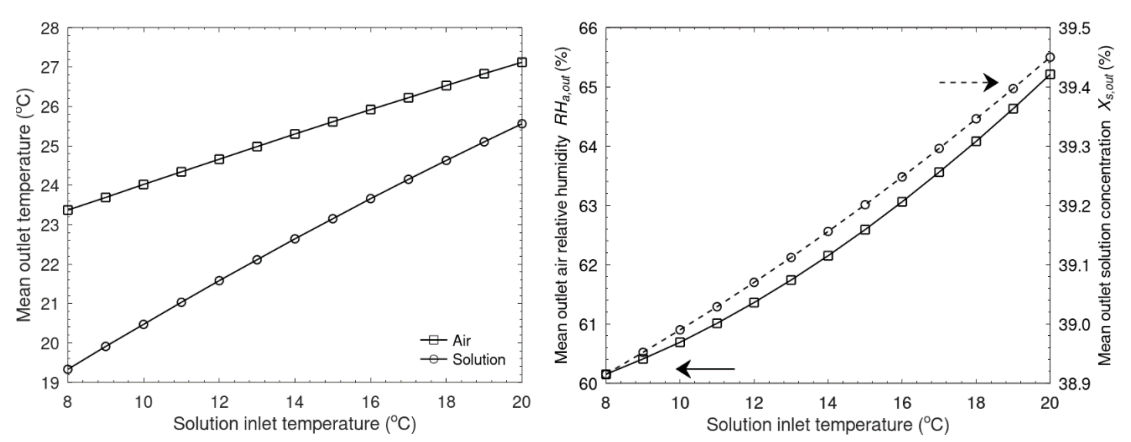


Figure 52 - Effect of solution inlet temperature on outlet air temperature/humidity and solution concentration

It is figured out from Figure 52 that both air and solution mean outlet temperatures increase with the surge of solution inlet temperature with the minimum and maximum temperature differences of 1.57°C and 4.04°C, respectively. Similarly, the relationship between solution inlet temperature and outlet air humidity shows the same variation trend as the former parameter. Both air and solution side outlet air humidity rise with the increasing solution inlet temperature.





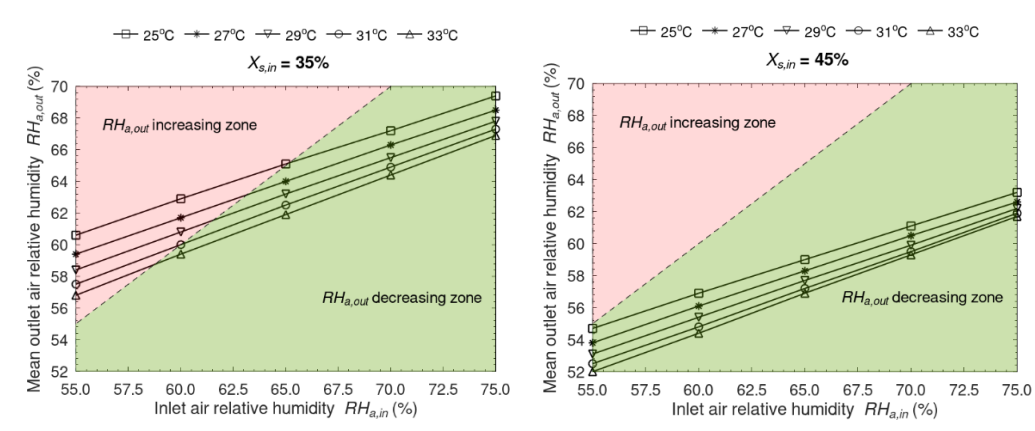


Figure 53 - Effect of solution concentration and inlet air temperature on outlet relative humidity.

The solution concentration has low impact on the outlet temperature of air. As the abovementioned descriptions in *Figure 53*, the increasing and decreasing zones are ascertained. **Erro! A origem da referência não foi encontrada.** illustrates the relations between the air inlet and outlet mean relative humidity under different solution concentration circumstances (35% and 45%). Albeit the increasing trends are identical to that of 40% concentration, the optimised solution concentration is chosen as 40% since the decreasing zone expands with the increasing concentration, which leads to higher expenses and more system complexities.

The thermal COP and Electrical COP with different inlet temperature and relative humidity are calculated with results in Table 16 and Table 17, respectively.

Table 16 Thermal COP for different inlet temperature and relative humidity

| | | - | | - | | |
|----------------|------|------|-----------------|------|------|------------|
| | | | $RH_{a,in}$ (%) | | | |
| $T_{a,in}$ | 55 | 60 | 65 | 70 | 75 | |
| 25 | 0.09 | 0.11 | 0.12 | 0.14 | 0.16 | |
| 27 | 0.12 | 0.14 | 0.16 | 0.18 | 0.20 | |
| 29 | 0.16 | 0.18 | 0.20 | 0.22 | 0.24 | COP_{th} |
| 31 | 0.19 | 0.22 | 0.24 | 0.26 | 0.29 | C.I.C |
| 33 | 0.23 | 0.26 | 0.29 | 0.31 | 0.34 | |

Table 17 Electrical COP for different inlet temperature and relative humidity.

| $T_{a,in}$ | 55 | 60 | 65 | 70 | 75 | |
|------------|------|------|------|------|------|--------------|
| 25 | 1.57 | 1.83 | 2.10 | 2.36 | 2.62 | |
| 27 | 2.07 | 2.37 | 2.66 | 2.96 | 3.25 | COP_{elec} |
| 29 | 2.61 | 2.94 | 3.27 | 3.60 | 3.92 | |
| | | | | | | - |



| 31 | 3.19 | 3.56 | 3.92 | 4.28 | 4.64 |
|----|------|------|------|------|------|
| 33 | 3.81 | 4.21 | 4.61 | 5.01 | 5.41 |

Moreover, the hybrid system COP formulation is correlated as the relation with both inlet air temperature and relative humidity as shown below and *Figure 54*.

$$COP = (0.0034 \times T_{a,in} - 0.0331) \times RH_{a,in} + (0.0929 \times T_{a,in} - 3.6587)$$

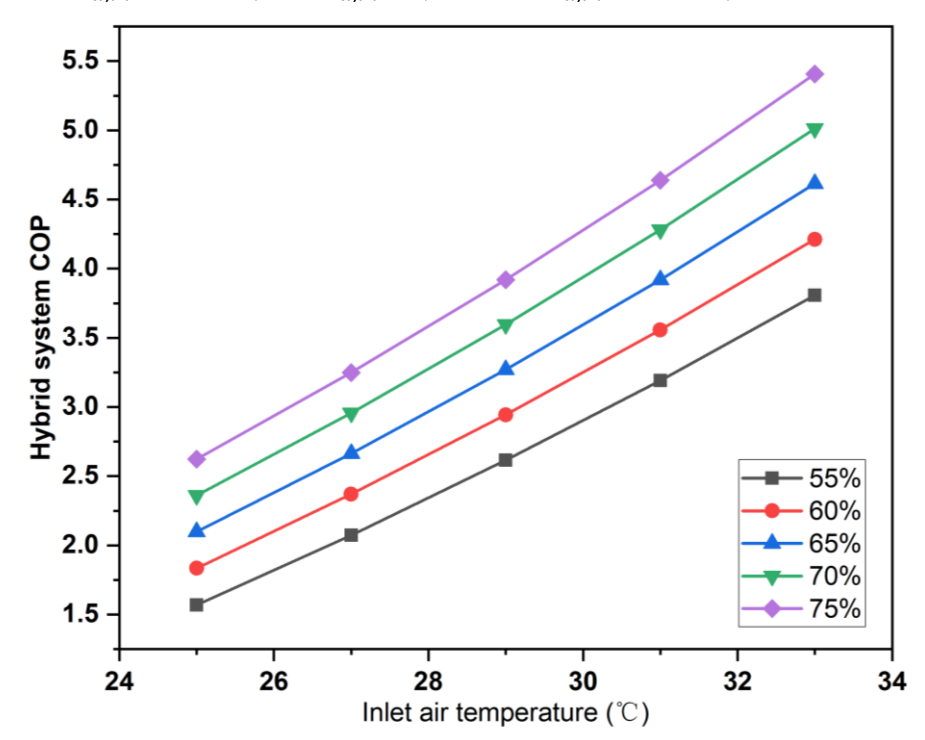


Figure 54 - Hybrid system COP with variables of inlet air temperature and relative humidity

4.7 Window heat recovery

The temperature distribution before and after each heat pipe measured during the experiments and obtained from the numerical model for four different test conditions are presented in *Figure 55*.



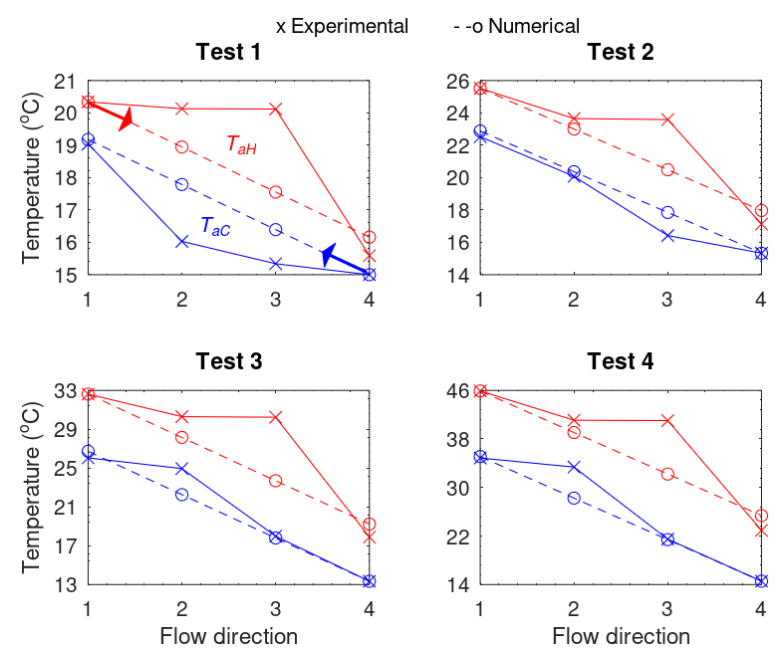


Figure 55 - Comparison between experimental and numerical results for different test conditions

There are some minor differences between measurements and numerical results, but it can be considered that the numerical model can predict reasonably the outlet temperature of air (the most important) on each side. The comparison between outlet temperature for the four test conditions obtained from experimental (Exp.) and numerical (Num.) are presented in *Table 18*.

Table 18 -Comparison between measured and modelled outlet temperature

| | Test 1 | | Test 2 | | Test 3 | | Test 4 | |
|------------------|--------|------|--------|------|--------|------|--------|------|
| | Exp. | Num. | Exp. | Num. | Exp. | Num. | Exp. | Num. |
| T_{aCin} (°C) | 15 | | 15.3 | | 13.4 | | 14.6 | |
| T_{aCout} (°C) | 19.0 | 19.2 | 22.5 | 22.9 | 26.0 | 26.7 | 34.9 | 35.1 |
| T_{aHin} (°C) | 20.4 | | 25.5 | | 32.6 | | 45.9 | |
| T_{aHout} (°C) | 15.6 | 16.2 | 17.1 | 18.0 | 17.9 | 19.2 | 22.9 | 25.4 |

According to the results presented in *Table 18*, the maximum difference between measured and modelled outlet temperature is always on the hot side, which are 3.8%, 5.3%, 7.3% and 10.9%, respectively, for tests 1, 2, 3 and 4. This difference increase when we increase the temperature range, which can be explained due to thermal losses not accounted for in the numerical model.

Temperature differences from 10 °C, 20 °C to 30 °C are investigated with the ventilation rates raised between 10 and 60 m³/h, as shown in *Figure 56*. It is figured out that the thermal effectiveness is similar in the range of 94.5% and 95.7% when a low ventilation rate of 10 m³/h. However, the thermal effectiveness decreases between 69.5% and 77.3% when the ventilation





rate rises to 60 m³/h. Thus, the thermal effectiveness declining rates are calculated as 0.06%/°C, 0.14%/°C, 0.22%/°C, 0.285%/°C, 0.345%/°C and 0.39%/°C with varied ventilation rates of 10 m³/h, 20 m³/h, 30 m³/h, 40 m³/h, 50 m³/h and 60 m³/h, respectively. Meanwhile, it is also figured out that the ventilation rates have the most significant impact on the improvement of thermal effectiveness, which reveals that the heat transfer coefficient has noticeable degradation with the rise of the ventilation rate from 10 m³/h to 60 m³/h. The thermal effectiveness is dropped by 18.4%, 22.4% and 25.0% with the rise of ventilation rate of 50 m³/h when the temperature differences are 10 °C, 20 °C and 30 °C, respectively.

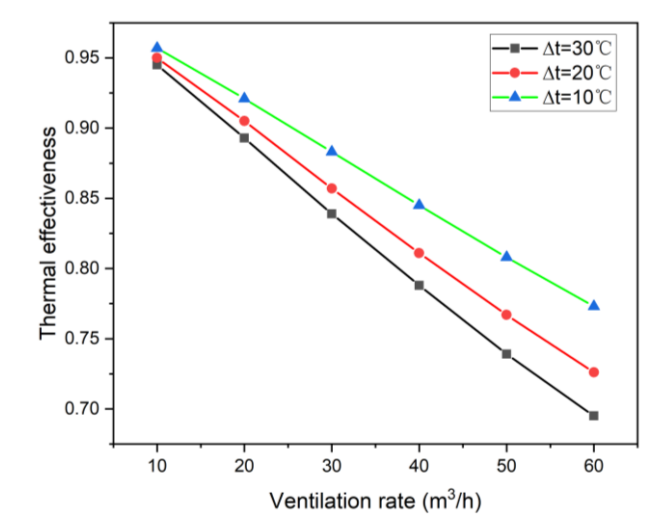


Figure 56 - Impact of maximum temperature difference on the thermal effectiveness with ventilation rate varied between 10 to 60 m³/h

It is figured out that the increase of heat pipe numbers has a significant impact on the improvement of thermal effectiveness, as shown in *Figure 57*, which reveals that the heat transfer coefficient has a noticeable upgrade when the heat pipe layers increase from $N_p=2$ to $N_p=3$, with total heat numbers increasing from 6 to 9. Results indicate that the thermal effectiveness is upgraded from 94.5% to 97.0% when a low ventilation rate of 10 m³/h. However, the thermal effectiveness decreased between 69.5% and 83.9% when the ventilation rate rises to 60 m³/h. Thus, the thermal effectiveness decreasing rates are calculated as 1.25%/layer, 2.6%/layer, 4.05%/layer, 5.25%/layer, 6.35%/layer and 7.2%/layer with varied ventilation rates of 10 m³/h, 20 m³/h, 30 m³/h, 40 m³/h, 50 m³/h and 60 m³/h, respectively.





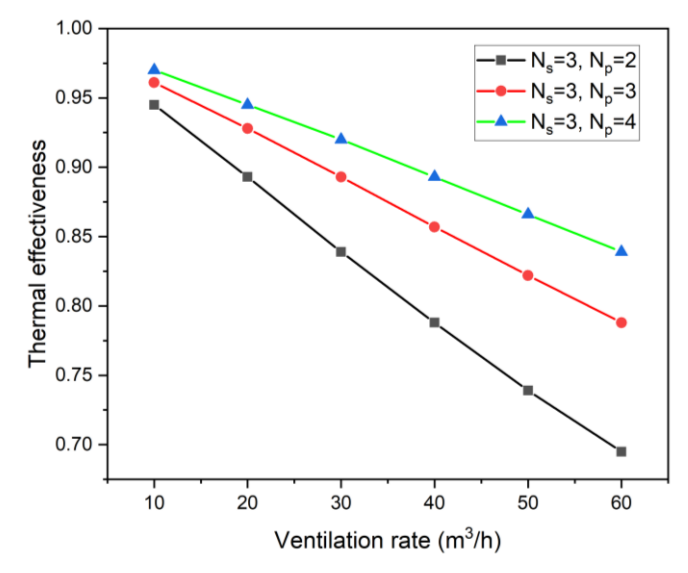


Figure 57 - Impact of heat pipe numbers on the thermal effectiveness with ventilation rate varied between 10 to 60 m³/h

4.8 Solar PV/T unit

Figure 58 presents the hourly variations of effective PV module temperature (T_{PV}) and water temperature Tw with the ambient temperature, Ta and incident solar radiation, I. It is shown that the PV module temperature throughout the operation remains higher than the water temperature as expected. The increase in water temperature circulating through the heat exchanger reaches up to 16°C throughout the testing. Figure 58 (b) illustrates the degree of polyethylene heat exchanger influence over the electric power conversion efficiency of the PV modules, Spv. For with Polyethylene HE case, the increase of cell efficiency as a result of passive cooling off via water circulation would lead to an increase on power conversion efficiency, Spv. On the other hand, higher cell temperature would cause a substantial decrease on the cell efficiency, Spv. Nevertheless, it was found that for both cases examined in this study, the cell efficiency, Spv is always better off with Poly HE case than without Poly HE case. This implies that from the viewpoint of the first law of thermodynamics, the "with Poly HE" case would be a better choice for PV systems to enhance the overall energy output of PV panels. Figure 58 (c) shows the variation of useful heat through circulating water with a mass flow rate of 0.0493 kg/s. The useful heat generated by the polyethylene heat exchanger roof unit ranges between 2.23 kW and 4.33 kW for the given test period.





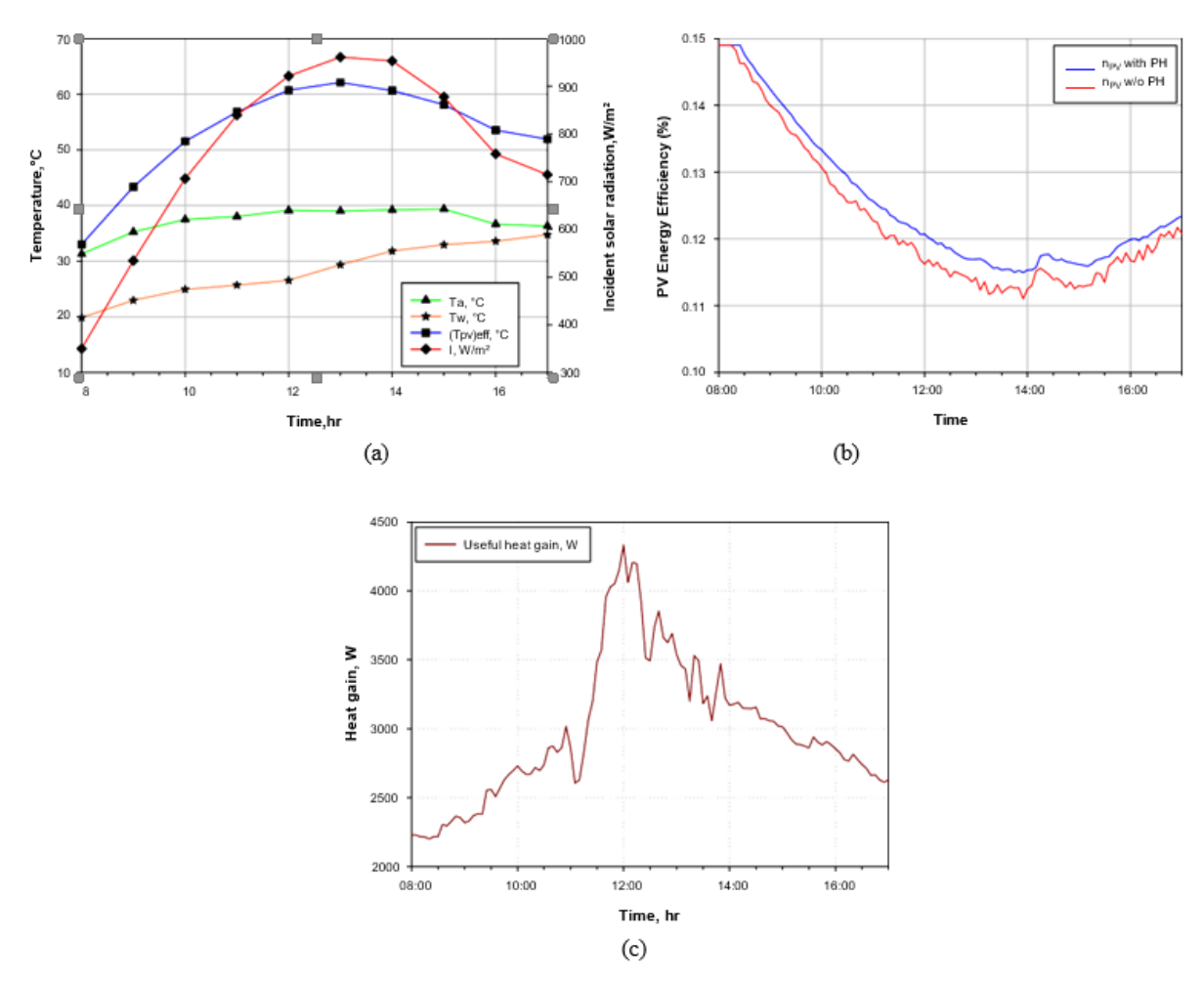


Figure 58 - a) Hourly variation of PV, ambient, water temperatures and incident solar radiation, b) effect of poly HE on power conversion efficiency and c) Useful heat gain

4.9 Prefabricated Panels

The U-values and R-values of the five PWI panels are calculated according to both experimental results and numerical calculation, with comparison conducted for validation, as shown in Table 19. According to Table 19, the error of U-value and R-value lie in the interval of 0.68 % to 6.39 % and 0.35 % to 6.04 %, respectively, indicating the accuracy of calculation results with maximum error less than 10 %. It is found that when combining the silicon aerogel wrapped by the breathable membrane, the R-value error of the Panel 3 is 0.35 % smaller than that without breathable membrane in Panel 4 and Panel 5, indicating a higher interior surface resistance and tighter air gaps existence due to well contact. Besides, for Panel 1, the combination of breathable membrane and VIP also have a lower R-value in experiment, also indicating a lower interior surface resistance and larger air gaps existence due to poor contact. However, Panel 2 and Panel 5 illustrate higher experiment performance with 2.47 % and 0.35 % error. By analysing the error and panel structures, it is figured out that both starch aerogel and silicon aerogel wrapped by the breathable membrane could improve the actual panel performance due to well contact between

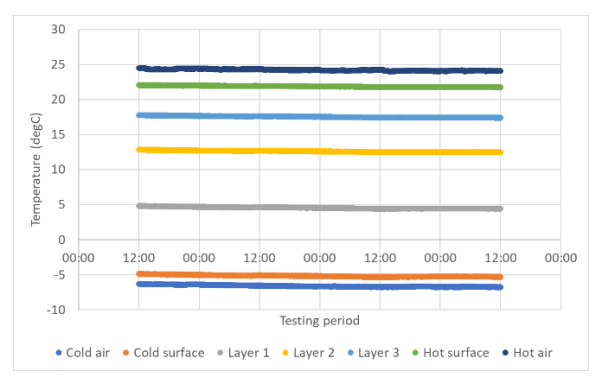


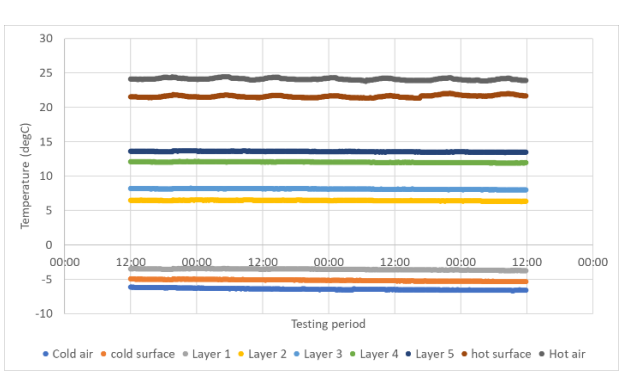


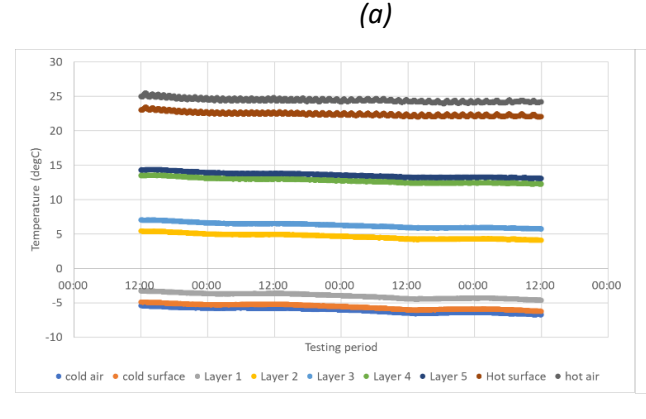
layers. Besides, the testing temperature distribution of 5 panels is shown in Figure 59. According to Figure 59, it is found that the highest internal surface temperature achieves 22 $^{\circ}$ C using Panel 1 with the core of VIP due to highest R-value (5.236 m²K/W) and the lowest achieves 8 $^{\circ}$ C using Panel 5 with the lowest R-value (2.816 m²K/W).

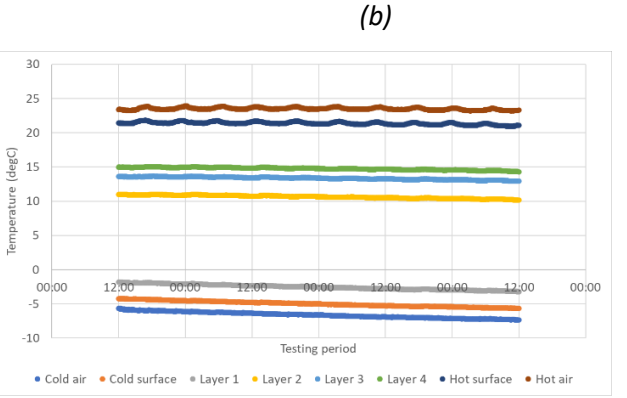
Table 19 - Validation of U and R values

| Panel 1 | Num. | Exp. | Error |
|------------------------------|-------|-------|-------|
| U-value (W/m ² K) | 0.181 | 0.191 | 5.52% |
| R-value (m ² K/W) | 5.524 | 5.236 | 5.21% |
| Panel 2 | Num. | Exp. | Error |
| U-value (W/m ² K) | 0.291 | 0.298 | 2.41% |
| R-value (m ² K/W) | 3.441 | 3.356 | 2.47% |
| Panel 3 | Num. | Exp. | Error |
| U-value (W/m ² K) | 0.294 | 0.296 | 0.68% |
| R-value (m ² K/W) | 3.399 | 3.387 | 0.35% |
| Panel 4 | Num. | Exp. | Error |
| U-value (W/m ² K) | 0.313 | 0.333 | 6.39% |
| R-value (m ² K/W) | 3.193 | 3 | 6.04% |
| Panel 5 | Num. | Exp. | Error |
| U-value (W/m ² K) | 0.335 | 0.355 | 5.97% |
| R-value (m ² K/W) | 2.986 | 2.816 | 5.69% |









(c) (d)





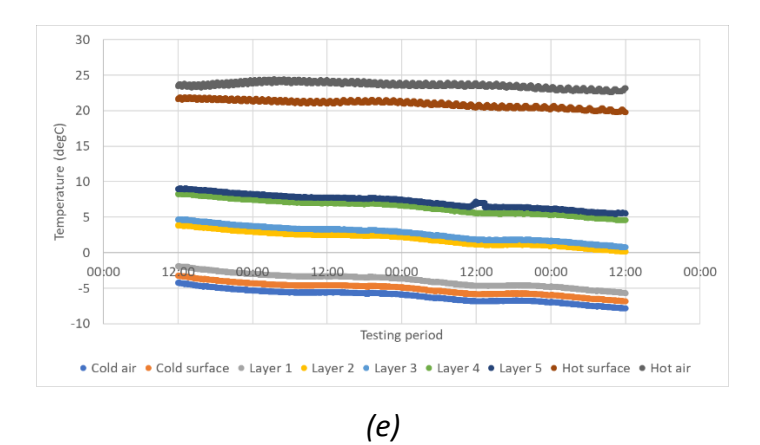


Figure 59 - Testing temperature distribution of (a) panel 1; (b) panel 2; (c) panel 3; (d) panel 4 and (e) panel 5





5. Conclusions

The innovative technologies have been tested under controlled conditions, including bio-aerogel insulation panel, PV vacuum glazing unit, PCM panel, solar-assisted heat pump, ground source heat pump, evaporative cooling unit, window heat recovery, solar PV/T unit and prefabricated panels. The achieved results were used to modify the design of technologies. Among them, the performances of the innovative technologies have been validated, with different climatic and operating conditions. Besides, the solar-assisted heat pump, ground source heat pump and evaporative cooling unit have been optimized with improved energy performance. This deliverable will be used for prototypes and real products manufacture and will be described in the deliverable D4.10.





References

- CHEN, X., SU, Y., AYDIN, D., DING, Y., ZHANG, S., REAY, D. & RIFFAT, S. 2018. A novel evaporative cooling system with a polymer hollow fibre spindle. *Applied Thermal Engineering*, 132, 665-675.
- CISTERNAS, L. A. & LAM, E. J. 1991. An analytic correlation for the vapour pressure of aqueous and non-aqueous solutions of single and mixed electrolytes. Part II. Application and extension. *Fluid Phase Equilibria*, 62, 11-27.